Title

Bruce suppresses autophagy-regulated caspase activity and wing tissue growth in *Drosophila*

Authors

Natsuki Shinoda[a,1], Yutaro Hama[b], Nozomi Hanawa[a] and Masayuki Miura[a,c,1]

Affiliations & Footnotes

[a]Department of Genetics, Graduate School of Pharmaceutical Sciences, The University of Tokyo, 7-3-1 Hongo, Bunkyo-ku, Tokyo 113-0033, Japan

[b]Institute for Genetic Medicine, Hokkaido University, Kita 15, Nishi 7, Kita-ku, Sapporo, Hokkaido, 060-0815, Japan

[c]Laboratory for Cell Vigor Regulation, National Institute for Basic Biology, Nishigonaka 38, Myodaiji, Okazaki, Aichi 444-8585, Japan

[1]Corresponding authors

Corresponding Authors

Natsuki Shinoda: Department of Genetics, Graduate School of Pharmaceutical Sciences, University of Tokyo 7-3-1 Hongo, Bunkyo-ku, Tokyo 113-0033, Japan. Telephone: +81-3-5841-4863. E-mail: f-shinoda.natsuki@g.ecc.u-tokyo.ac.jp

Masayuki Miura: Laboratory for Cell Vigor Regulation, National Institute for Basic Biology, Nishigonaka 38, Myodaiji, Okazaki, Aichi 444-8585, Japan. Telephone: +81-564-55-7650. E-mail: miura@nibb.ac.jp

Abstract

Caspases are cysteine-aspartic proteases that mediate both lethal and non-lethal cellular outcomes, including the promotion of tissue growth. However, the mechanisms underlying the differential regulation of these activities remain unclear. We have previously shown that among the two *Drosophila* executioner caspases, Dcp-1 and Drice, Dcp-1 promotes tissue growth in a non-lethal manner, independent of canonical apoptotic signaling. Herein, we demonstrated that overexpressed Dcp-1, but not Drice, was activated without canonical apoptosome components. TurboID-based proximity labeling revealed distinct proximal proteomes, among which Sirtuin 1, an Atg8a deacetylase, which promotes autophagy, was specifically required for Dcp-1 activation. Autophagy-related genes, including Bcl-2 family members *Debcl* and *Buffy*, are required for Dcp-1 activation. Structure-based prediction using AlphaFold3 further identified Bruce, an autophagy-regulated inhibitor of apoptosis, as a Dcp-1-specific regulator acting outside the apoptosome-mediated pathway. Physiologically, Bruce suppresses wing tissue growth. These findings indicate that non-lethal Dcp-1 activity is governed by the autophagy-Bruce axis, enabling distinct non-lethal functions independent of cell death.

Keywords

Autophagy, Caspase, Drosophila, tissue growth, TurboID

43 **Introduction**

44 Caspases are cysteine-aspartic acid proteases that serve as the central executioners of apoptosis.
45 In *Drosophila*, core caspase-mediated signaling for apoptosis is well conserved (Nakajima &
46 Kuranaga, 2017; Shinoda & Miura, 2024). Upon apoptotic stimulation, the pro-apoptotic genes
47 *rpr*, *hid*, and *grim* (*RHG*), which antagonize DIAP-1, an inhibitor of apoptosis protein (IAP),
48 are transcriptionally upregulated. The degradation of DIAP-1 allows the initiator caspase Dronc
49 and its activator Dark to assemble into the apoptosome, thereby triggering a proteolytic cascade
50 that activates the executioner caspases Dcp-1 and Drice, ultimately leading to apoptosis. In
51 addition to their role in apoptosis, caspases perform diverse non-cell death functions
52 collectively termed caspase-dependent non-lethal cellular processes (Aram *et al*, 2017).
53 However, the mechanisms that differentially regulate lethal and non-lethal caspase activity
54 remain largely unknown.

55 Functional specificity appears to arise at the level of the executioner caspases. Of the
56 two executioner caspases in *Drosophila*, Drice is more potent than Dcp-1 in inducing cell death
57 in wing imaginal discs (Florentin & Arama, 2012). In contrast, Dcp-1 is required for autophagy
58 triggered by starvation or proteasome dysfunction in the ovaries (Hou *et al*, 2008; DeVorkin *et*
59 *al*, 2014; Choutka *et al*, 2017). We have previously demonstrated that Dcp-1, but not Drice,
60 specifically promotes imaginal tissue growth independent of apoptosome and cell death
61 (Shinoda *et al*, 2019). Mechanistically, we showed that cleavage-mediated inactivation of
62 Acinus, a positive regulator of autophagy (Nandi *et al*, 2014; Haberman *et al*, 2010), which
63 limits tissue growth independently of autophagy (Tyra *et al*, 2020), partly promotes tissue
64 growth (Shinoda *et al*, 2019). However, the upstream regulatory mechanisms that selectively
65 regulate Dcp-1 activity remain unknown.

66 Proximity labeling has emerged as a powerful approach for comprehensively analyzing
67 molecular interactions, including protein-protein interactions (Qin *et al*, 2021). TurboID

68 enables the rapid biotinylation of lysine residues on neighboring proteins within 10 minutes in
69 cultured cells (Branon *et al*, 2018). Streptavidin-based enrichment of these biotinylated proteins,
70 followed by mass spectrometry, allows the proteome-wide identification of proteins near a
71 target of interest. We previously generated *Drosophila* lines in which TurboID was knocked in
72 at the C-termini of Dronc, Dcp-1, or Drice (Shinoda *et al*, 2019). In wing imaginal discs,
73 TurboID-based labeling has revealed distinct proximity patterns for Dcp-1 and Drice,
74 suggesting that each executioner caspase is associated with a unique set of neighboring proteins
75 (Shinoda *et al*, 2019). We have shown that the differences in substrate specificity between Dcp-
76 1 and Drice were consistent with their distinct proximity profiles in the ovary, as exemplified
77 by BubR1 (Shinoda *et al*, 2023). Moreover, overexpression of *Fasciclin 3*, a Drice-proximal
78 protein identified in adult brains, induces non-lethal caspase activation in a Dronc-dependent
79 manner (Muramoto *et al*, 2025). These findings indicate that caspase-proximal proteins can
80 function not only as potential substrates but also as regulatory factors.
81 In this study, we investigated the regulatory mechanisms underlying Dcp-1 activation.
82 We found that the overexpression of *Dcp-1* induced a wingless phenotype. Using this
83 phenotype as a functional readout, we found that Dcp-1 activation specifically requires its
84 proximal protein Sirtuin 1 (Sirt1), Bcl-2 family members Debcl and Buffy, and components of
85 the autophagy pathway. Notably, the autophagy-regulated giant IAP Bruce specifically
86 interacts with and regulates Dcp-1 activity without affecting apoptosome-mediated core
87 apoptotic signaling, thereby suppressing wing imaginal tissue growth. Together, these findings
88 reveal that Bruce acts upstream to diverge the regulatory pathways of Dcp-1 and Drice, enabling
89 Dcp-1 to mediate distinct non-lethal functions through autophagy, independent of cell death.
90

Results

Overexpression of Dcp-1, but not Drice, induces apoptosis

Structurally, the executioner caspases, Dcp-1 and Drice, are similar, each comprising catalytic P20 and P10 domains and a highly disordered N-terminal prodomain (Fig. 1A). First, we assessed the ability of two executioner caspases to trigger apoptosis. Using the *WP-Gal4* driver, the overexpression of *Dcp-1* resulted in a wingless phenotype indicative of apoptotic cell death, whereas the overexpression of *Drice* did not (Fig. 1B), which is consistent with our previous observations in olfactory receptor neurons (Muramoto *et al*, 2025). Next, we examined the apoptotic potential of fluorescently tagged caspases in *Drosophila* S2 cells expressing mNeonGreen (mNG)-fused Dcp-1 or Drice. Dcp-1 expression caused a marked reduction in mNG intensity (Fig. EV1A–C) and a decreased number of mNG-positive cells (Fig. EV1A, D). These effects required Dcp-1 catalytic activity, as the mutation of the catalytic cysteine to glycine restored both mNG intensity and cell number (Fig. EV1A–D). In contrast, Drice expression neither reduced mNG intensity nor decreased the number of mNG-positive cells, resembling the catalytically inactive mutant (Fig EV1A–D). Taken together, these results demonstrate that Dcp-1, but not Drice, is activated upon overexpression and induces apoptosis in multiple cell types.

Dcp-1 activation is independent of the apoptosome composed of Dronc and Dark

Executioner caspases are typically activated by cleavage mediated by the initiator caspase, Dronc, which is activated through the assembly of the Dark-dependent apoptosome (Fig. 1C) (Nakajima & Kuranaga, 2017; Shinoda & Miura, 2024). We previously proposed that Dcp-1 can be activated independently of Dark and Dronc (Shinoda *et al*, 2019). To test this hypothesis further, we analyzed genetic modifiers of the Dcp-1-induced wingless phenotype. A heterozygous mutation in the *H99* deficiency, which encompasses the pro-apoptotic *reaper*, *hid*,

116 and *grim* (*RHG*) genes, rescued the wingless phenotype caused by *Dcp-1* overexpression (Fig.
117 1D, F). Similarly, expression of the caspase inhibitor *p35* or knockdown of *RHG* genes also
118 rescued this phenotype (Fig. 1E, F), suggesting that Dcp-1 induces apoptosis in a catalytic
119 activity-dependent manner under the control of RHG proteins. In contrast, knockdown of other
120 core apoptotic components, including Dark, Dronc, and Drice, or overexpression of the
121 dominant-negative form of Dronc ($Dronc^{DN}$) failed to suppress the wingless phenotype (Fig.
122 1E, F). These findings support our earlier observation that Dcp-1 can be activated independent
123 of the canonical apoptosome composed of Dronc and Dark to mediate non-lethal functions
124 (Shinoda *et al*, 2019). Collectively, these results indicate that, at least under overexpression
125 conditions, Dcp-1 activation proceeds independently of the apoptosome, in contrast to that of
126 Drice.
127
128 ***Dcp-1 and Drice show distinct expression patterns among tissues***
129 Proximal proteins of caspases have emerged as potential regulators of executioner caspase
130 activity (Muramoto *et al*, 2025). We have previously demonstrated that the proximal protein
131 patterns of Dcp-1 and Drice differ even within the same tissue, such as wing imaginal discs
132 (Shinoda *et al*, 2019). Based on this, we sought to identify Dcp-1-specific regulatory factors
133 among its proximal proteins. First, we examined the tissue distribution of *Drosophila* caspases
134 using previously established *Caspase::V5::TurboID* knock-in fly lines (Shinoda *et al*, 2019).
135 Expression patterns were analyzed in larval tissues, including the salivary glands, fat bodies,
136 and brain (Fig. EV2A), with confirmed expression in wing imaginal discs (Fig. 2A) as well as
137 in adult tissues, including the thorax, ovary, and testis (Fig. EV2B). Drice was ubiquitously
138 expressed in all examined tissues. In contrast, Dcp-1 expression was restricted to the larval
139 brain and adult ovaries and testes.
140

141 ***Drosophila executioner caspases associate with distinct sets of proximal proteins***

142 Next, we compared the proximal protein profiles of *Drosophila* executioner caspases, based on
143 our previous observation that Dcp-1 and Drice are associated with distinct sets of proximal
144 proteins, potentially reflecting differences in their activation mechanisms (Shinoda *et al*, 2019).
145 Streptavidin staining, used to visualize proteins biotinylated via TurboID-mediated proximity
146 labeling, revealed distinct patterns of Dcp-1 and Drice expression across tissues (Figs. 2A and
147 EV2A, B). To directly compare their proximal landscapes in the same cellular context, we
148 focused on the imaginal discs. NeutrAvidin-based purification of biotinylated proteins,
149 followed by mass spectrometry, identified 818 proteins (Fig. 2B, C). As expected, the proximal
150 proteomes of Dcp-1 and Drice were distinct. BubR1 and Fasciclin 3 isoform G, previously
151 identified as Drice-proximal in adult brain and ovary tissues (Shinoda *et al*, 2023; Muramoto
152 *et al*, 2025), were enriched in the Drice-associated proteome (Fig. 2C, Table EV1), suggesting
153 that Drice maintains its proximity to specific partners across tissues. Among the top Dcp-1-
154 enriched proximal proteins was the chaperonin containing TCP1 subunit 8 (CCT8). To validate
155 these findings, we generated an antibody against CCT8 (Fig. 2D). Western blotting confirmed
156 the presence of CCT8 in Dcp-1::V5::TurboID samples but not in Drice::V5::TurboID samples
157 (Fig. 2E). Taken together, these results show that, even when expressed at comparable levels
158 in the same tissue, Dcp-1 and Drice are associated with distinct sets of proximal proteins, which
159 is consistent with their differential regulation and functional specificity.

160

161 ***Screening of Dcp-1 proximal proteins identifies Sirt1 as a Dcp-1-specific activator***

162 To identify potential regulators of Dcp-1 activation, we performed an RNAi screen targeting
163 eight genes that were selectively proximal to Dcp-1 relative to Drice and wild-type controls
164 (Dcp-1/Drice fold change > 1.5, Dcp-1/Control fold change > 10 and PSM ≧ 2; Table EV1),
165 using two independent RNAi lines per gene (Fig. 2F). Under normal conditions, RNAi-

166 mediated knockdown of the chaperonin components *CCT2* and *CCT8* resulted in a wingless
167 phenotype, whereas knockdown of other genes had no effect (Fig. EV3A). Under *Dcp*-1
168 overexpression conditions, knockdown of *Fkbp59* or *Sirt1* partially suppressed Dcp-1-induced
169 cell death (Fig. 2G, Fig. EV3B). The requirement for Sirt1 was further confirmed using a
170 transheteroallelic combination of two previously described *Sirt1* deletion alleles, $Sirt1^{2A-7-11}$
171 (Xie & Golic, 2004; Furuyama *et al*, 2004) and $Sirt1^{4.5}$ (Newman *et al*, 2002), which
172 significantly rescued the wingless phenotype (Fig. 2H, I). These results indicate that the Dcp-
173 1-proximal protein Sirt1 is required for Dcp-1 activation upon overexpression.
174
175 ***Dcp-1 activation specifically depends on Debcl, Buffy, and autophagy***
176 Sirt1, also known as dSir2, is a lysine deacetylase that promotes the expression of autophagy-
177 related genes via Atg8a deacetylation under starvation (Jacomin *et al*, 2020). Multiple studies
178 have linked Dcp-1 to the regulation of autophagy. Dcp-1, together with the Bcl-2 family
179 proteins Debcl and Buffy, but not Drice, has been shown to be required for starvation-induced
180 autophagy in *Drosophila* l(2)mbn cells (Hou *et al*, 2008), and Dcp-1 is also required for
181 autophagy in the ovary (Hou *et al*, 2008; DeVorkin *et al*, 2014; Choutka *et al*, 2017). More
182 recently, the BH3-only protein Sayonara (Synr) was reported to induce Dcp-1-dependent cell
183 death, which is regulated by Debcl, Buffy, and autophagy (Ikegawa *et al*, 2023). In contrast, a
184 gain-of-function modifier screen revealed that autophagy antagonizes Dcp-1-induced cell death
185 (Kim *et al*, 2010) and that Dcp-1 suppresses autophagy through cleavage-mediated inactivation
186 of Acinus (Haberman *et al*, 2010; Nandi *et al*, 2014).
187 Based on these reports, we examined whether Synr, Debcl, Buffy, and core autophagy
188 components regulate Dcp-1 activation. Knockdown of *Synr* did not suppress Dcp-1-induced
189 cell death, whereas knockdown of *Debcl* or *Buffy* significantly rescued this wingless phenotype
190 (Fig. 3A, B). Similarly, knockdown of the autophagy-related genes *Atg2* and *Atg8a* suppressed

191 Dcp-1-induced cell death (Fig. 3A, B), indicating that Debcl, Buffy, and autophagy are required
192 for Dcp-1 activation. To assess the specificity of these regulators, we analyzed the eye ablation
193 phenotype caused by overexpression of *Hid*, which triggers apoptosis via canonical apoptotic
194 signaling. As expected, this phenotype was rescued by *p35* expression or knockdown of *RHG*
195 genes and partially suppressed by inhibition of the Dark-, Dronc-, and Drice-dependent
196 apoptosome pathways (Fig. 3C), confirming its dependence on canonical apoptosis (Fig. 1C).
197 In contrast, *Hid*-induced apoptosis was not rescued by RNAi against *Dcp-1* (Fig. 3C), nor by
198 knockdown of *Sirt1* or *Fkbp59* (Fig. 3D). Furthermore, knockdown of *Debcl*, *Buffy*, and
199 autophagy genes failed to rescue *Hid*-induced apoptosis (Fig. 3E). Taken together, these results
200 indicate that Sirt1, Debcl, Buffy, and autophagy components are not general regulators of
201 apoptosis but function as specific activators of Dcp-1.
202
203 ***Cleaved Dcp-1 specifically interacts with a giant-IAP Bruce***
204 Next, we examined the molecular link between autophagy and Dcp-1 activation. Caspase
205 activation is negatively regulated by IAPs. In *Drosophila*, DIAP1 suppresses caspase activity
206 through ubiquitination (Ditzel *et al*, 2008) (Fig. 1C). In addition to DIAP1, *Drosophila* has
207 another giant IAP, *Bruce*, which is degraded via autophagy during oogenesis (Nezis *et al*, 2010).
208 Bruce inhibits autophagy under nutrient-rich conditions (Hou *et al*, 2008), suggesting mutual
209 negative regulation of Bruce and autophagy. Bruce selectively inhibits *reaper*-induced cell
210 death, but not *hid*-induced apoptosis, suggesting a degree of pathway specificity (Domingues
211 & Ryoo, 2012). These observations led us to focus on Bruce as a potential selective regulator
212 of Dcp-1 activation.
213 The structure of human Bruce/BIRC6 has recently been resolved using cryo-electron
214 microscopy (Hunkeler *et al*, 2023; Ehrmann *et al*, 2023; Liu *et al*, 2024; Dietz *et al*, 2023),
215 revealing several conserved domains: linker domain (LD), baculoviral IAP repeat (BIR), WD40,

216 β-X1, β-X2, carbohydrate-binding module (CBM), ubiquitin-like (UBL), and ubiquitin-
217 conjugating (UBC) (Fig. 4A). Human Bruce/BIRC6 ubiquitinates the activated executioner
218 caspases caspase-3 and caspase-7, but not their non-processed proforms *in vitro* (Dietz *et al*,
219 2023). The BIR domain mediates interactions with ubiquitination substrates by recognizing N-
220 terminal IAP-binding motifs (IBMs) (Berthelet & Dubrez, 2013). The consensus IBM sequence
221 is defined as A(K/T/V/I)(P/A/E)(F/E/I/S/Y) (Vaux & Silke, 2005). We identified IBM-like
222 sequences at the N-termini of the P20 domains of both Dcp-1 and Drice (Fig. 4B, C). To assess
223 the potential interaction between Bruce and these caspases, we used AlphaFold3 to predict the
224 structure of the complexes between Bruce and the IBM-like motifs of Dcp-1 and Drice
225 (Abramson *et al*, 2024). Consistent with the known architecture of BIRC6, AlphaFold3
226 predicted that the BIR domain of Bruce interacts with LD, WD40, β-X1, and β-X2 domains
227 (Fig. EV4A, B). For structural prediction, we used a Bruce fragment spanning residues 1–1960,
228 including the BIR domain and its associated Zn^{2+}-binding site (Fig. 4A), and 15-residue
229 peptides from the Dcp-1 and Drice cleavage sites encompassing their IBM-like motifs (Fig. 4B,
230 C). The predicted structures revealed a high-confidence interaction between Dcp-1 and the
231 Bruce BIR domain. All five AlphaFold3 models showed confident pLDDT scores (70–90) for
232 the N-terminal residues of Dcp-1, corresponding to the IBM-like motif (Fig. 4D, F). The
233 predicted binding mode resembled the canonical BIR-IBM interaction observed in XIAP BIR3-
234 Smac (Wu *et al*, 2000) (Fig. EV4C). In contrast, although Drice appeared to bind to Bruce in
235 the predicted models, the pLDDT scores were consistently low (<70) across the interaction
236 interface, including the four N-terminal residues, indicating low confidence in the predicted
237 interaction (Fig. 4E, G).

238 To validate these predictions, we performed co-immunoprecipitation assays on
239 *Drosophila* S2 cells. We found that only the cleaved form of Dcp-1, which forms a head-to-tail
240 dimer composed of the P20 and P10 domains (Julien & Wells, 2017), and not the full-length

241 protein, interacted with the N-terminal BIR domain of Bruce following apoptosis induction (Fig.
242 4H), consistent with the observation that human Bruce/BIRC6 only targets cleaved executioner
243 caspases for ubiquitination *in vitro* (Dietz *et al*, 2023). Conversely, neither the cleaved nor full-
244 length forms of Drice showed detectable interactions with the Bruce BIR domain (Fig. 4H),
245 corroborating the AlphaFold3 predictions. Taken together, these findings suggest that Bruce
246 specifically suppresses activated Dcp-1 but not Drice and serves as a branching point for a Dcp-
247 1-specific, non-canonical regulatory pathway.
248
249 ***Bruce is ubiquitously expressed in wing imaginal discs***
250 Bruce has been reported to function in oogenesis and spermatogenesis in the ovaries and testes,
251 respectively (Arama *et al*, 2003, 2007; Kaplan *et al*, 2010; Nezis *et al*, 2010; Hou *et al*, 2008).
252 However, its expression in other tissues has not been thoroughly characterized. To examine the
253 tissue distribution of Bruce, we generated CRISPR/Cas9-mediated knock-in flies in which an
254 mStayGold::C4 linker::V5-tag (Ando *et al*, 2024) was inserted into the N-terminus of Bruce
255 (Fig. EV5A). Using the knocked-in line, we confirmed that Bruce was expressed in the ovaries
256 (Fig. EV5B) and testes (Fig. EV5C), consistent with previous reports (Arama *et al*, 2003, 2007;
257 Kaplan *et al*, 2010; Nezis *et al*, 2010; Hou *et al*, 2008). Western blot analysis revealed Bruce
258 expression in both adult males and females (Fig. EV5D). We also detected Bruce expression in
259 wing imaginal discs (Fig. EV5E). This signal was abolished by the RNAi-mediated knockdown
260 of *Bruce*, confirming the specificity of the signal (Fig. EV5F). These findings indicate that
261 Bruce not only functions in the gonads but can also exert Dcp-1 regulatory functions in wing
262 imaginal discs.
263
264 ***Bruce specifically suppresses Dcp-1 overexpression-induced cell death***

265 Next, we investigated whether Bruce regulated Dcp-1 activity. Upon overexpression of *Bruce*
266 (Fig. 5A), we observed marked suppression of Dcp-1-induced cell death (Fig. 5B, C). Although
267 *DIAP1* overexpression also inhibited Dcp-1 activation, this suppressive effect was stronger
268 following *Bruce* overexpression (Fig. 5B, C). We examined the specificity of Bruce in the
269 regulation of other forms of cell death. As mentioned earlier, the BH3-only protein Synr induces
270 autophagy and Dcp-1-dependent cell death (Ikegawa *et al*, 2023). To investigate whether Bruce
271 was involved in Debcl/Buffy-autophagy-Dcp-1-mediated cell death, we examined the role of
272 Bruce in Synr-induced cell death. Overexpression of *Bruce*, but not *DIAP1*, specifically
273 suppressed Synr-induced cell death (Fig. 5D). In contrast, *Bruce* overexpression failed to rescue
274 the eye ablation phenotype independent of autophagy caused by *Hid* overexpression, whereas
275 DIAP1 fully rescued this phenotype (Fig. 5E). Taken together, these results suggest that Bruce
276 and DIAP1 regulate distinct cell death pathways, with Bruce acting as a selective inhibitor of
277 autophagy-regulated Dcp-1- and Synr-dependent cell death.
278
279 ***Bruce suppresses wing tissue growth***
280 We have previously reported that Dcp-1 activity can promote imaginal tissue growth
281 independent of the core apoptosis signaling pathway, including Dronc (Shinoda *et al*, 2019).
282 To investigate the role of Bruce in imaginal tissue growth, we analyzed its effect on wing
283 imaginal discs using *WP-Gal4*, which drives expression throughout the wing pouch.
284 Overexpression of *p35* suppressed wing tissue growth (Fig. 5F, G), whereas inhibition of
285 canonical apoptotic signaling by $Dronc^{DN}$ and *DIAP1* had no effect (Fig. 5F, G). In contrast,
286 *Bruce* overexpression suppressed wing growth to an extent similar to *p35* overexpression,
287 whereas *Bruce* knockdown tended to increase wing size, although the difference was not
288 statistically significant (Fig. 5F, G). We confirmed these results using *Engrailed-Gal4*, which
289 is expressed in the posterior compartment of the wing imaginal disc. *p35* overexpression

290 suppressed wing tissue growth (Fig. 5H, I). In this context, the inhibition of canonical apoptosis
291 signaling by *Dronc*^{DN} and *DIAP1* had a minor but negative effect on wing size (Fig. 5H, I).
292 *Bruce* overexpression suppressed wing growth, whereas *Bruce* knockdown increased wing size
293 (Fig. 5H, I), indicating that Bruce negatively regulates wing tissue growth. Finally, to enhance
294 the sensitivity of the assay, we overexpressed the dominant-negative form of the insulin
295 receptor (*InR*^{DN}) using *WP-Gal4*, which significantly reduced wing size (Fig. 5J, K). Under this
296 sensitized condition, simultaneous *Bruce* knockdown significantly enhanced wing tissue
297 growth (Fig. 5J, K). Overall, these results indicate that Bruce suppresses wing tissue growth.
298

299 **Discussion**

300 ***Autophagy-facilitated alternative caspase activation pathway***

301 In this study, we identified a distinct regulatory mechanism governing the activation of the
302 *Drosophila* executioner caspase, Dcp-1, in sharp contrast to its paralog Drice. Although both
303 caspases share structural similarities and are expressed in overlapping tissues, Dcp-1, but not
304 Drice, is activated upon overexpression in an apoptosome-independent, autophagy-regulated
305 manner. Previous studies have implicated Dcp-1 in the induction of autophagy (Hou *et al*, 2008;
306 DeVorkin *et al*, 2014; Choutka *et al*, 2017). Our findings extend this view by showing that
307 autophagy is required for Dcp-1 activation, suggesting a positive feedback loop between Dcp-
308 1 and autophagy during apoptosis. Although the precise downstream targets of the Bcl-2 family
309 proteins, Debcl and Buffy, remain unknown, their roles in autophagy regulation (Hou *et al*,
310 2008) suggest that they influence Dcp-1 activity through autophagic pathways. Additionally,
311 we identified Bruce, a giant inhibitor of apoptotic proteins, as a Dcp-1-specific suppressor.
312 Functionally, Bruce limits wing tissue growth, suggesting that Dcp-1 activation contributes to
313 growth regulation in a non-lethal manner (Shinoda *et al*, 2019). Taken together, our results
314 demonstrate that the regulatory mechanisms of Dcp-1 and Drice diverge at the level of IAPs
315 and that Dcp-1 activation is regulated by autophagy, enabling specific non-lethal functions that
316 promote tissue growth independent of canonical apoptotic signaling (Fig. 5L). It is important
317 to note that Dcp-1 can also suppress autophagy through cleavage of Acinus (Haberman *et al*,
318 2010; Nandi *et al*, 2014). Although this may seem contradictory, the ability of caspases to
319 function in a non-lethal manner requires strict prevention of excessive activation. Such
320 suppression may represent a key mechanism that enables non-lethal caspase activity.

321 It is also important to understand how cells determine the usage of canonical versus
322 alternative caspase activation pathways depending on physiological or environmental
323 conditions. In mammals, two major apoptotic pathways are activated by distinct initiator

324 caspases, caspase-8 and caspase-9, in response to different upstream signals (Newton *et al*,
325 2024). Similarly, in *Drosophila*, while most developmental cell death is driven by canonical
326 apoptotic signaling involving Dronc (Xu *et al*, 2005), alternative caspase activation pathways
327 may be preferentially engaged in response to environmental stimuli, such as starvation or heat
328 shock.
329
330 ***Initiator caspase-independent activation mechanism for Dcp-1***
331 The mechanism by which Dcp-1 is activated by itself remains an open and important question.
332 In contrast to Drice, Dcp-1 is activated upon overexpression in an apoptosome-independent but
333 autophagy-dependent manner. Unlike initiator caspases, executioner caspases such as Dcp-1
334 generally lack long N-terminal prodomains and require proteolytic cleavage to become
335 catalytically active. Proximity-labeling analysis revealed that Dcp-1 was predominantly
336 associated with the chaperonin subunit CCT8 (Fig. 2E). Given that the overexpression of *Dcp-*
337 *1* increases its local concentration for activation, we propose that its accumulation in the
338 chaperonin complex may serve as a local scaffold for caspase activation. This model implies a
339 spatially restricted mode of regulation in which caspase activity is compartmentalized within
340 the cell. In this model, we speculated that Dcp-1 activation occurs sporadically in subcellular
341 regions enriched in activators or scaffolding molecules such as CCT8. Under these conditions,
342 Dcp-1 activation may need to be tightly regulated to prevent its unintended proteolytic activity.
343 Supporting this notion, we proposed that Bruce functions as a basal suppressor of Dcp-1 in non-
344 lethal contexts, restraining caspase activity when full apoptotic signaling is not engaged.
345
346 ***Distinct roles of evolutionarily multiplicated executioner caspases***
347 Caspases are essential cysteine proteases that execute apoptotic cell death and are conserved
348 from *C. elegans* to mammals (Shinoda & Miura, 2024). Multiple executioner caspases exist,

349 including caspase-3 and caspase-7 in mammals and Dcp-1 and Drice in *Drosophila*. Although
350 these enzymes are often functionally redundant in apoptosis, growing evidence indicates that
351 each executioner caspase harbors distinct substrate specificities and fulfills non-overlapping
352 roles (Walsh *et al*, 2008; Boucher *et al*, 2012; Desroches & Denault, 2019; Shinoda *et al*, 2019,
353 2023). In mammals, caspase-3 and caspase-7 exhibit high sequence similarity but differ in their
354 substrate preferences. Caspase-7, for instance, contains polybasic residues in its exosite that
355 enhance its ability to cleave RNA-binding proteins, a function not observed in caspase-3
356 (Boucher *et al*, 2012). Mechanistically, this exosite enables caspase-7 to interact directly with
357 RNA, thereby promoting selective proteolysis of RNA-associated substrates (Desroches &
358 Denault, 2019). Furthermore, we have recently demonstrated that caspase-7 is essential for
359 early-peaking caspase activity at the plasma membrane during apoptosis, a process mediated
360 by its N-terminal intrinsically disordered region, which facilitates rapid efferocytosis of
361 apoptotic cells (Taira *et al*, 2025). In this study, we demonstrated that *Drosophila* executioner
362 caspases Dcp-1 and Drice are also subject to distinct activation mechanisms for the specific
363 non-lethal function of tissue growth. These findings underscore that the evolutionary expansion
364 of executioner caspases does not merely provide functional redundancy for apoptotic execution
365 but rather confers unique biochemical properties and regulatory roles under distinct cellular
366 contexts. This diversification allows executioner caspases to participate in both lethal and non-
367 lethal cellular processes, highlighting their broader functional repertoire beyond canonical
368 apoptosis.
369

370 **Methods**

371 ***Fly strains and rearing conditions***

372 We raised the flies in standard *Drosophila* medium at 25°C. For in vivo biotin labeling
373 experiments, flies were raised in standard *Drosophila* medium supplemented with 100 μM (+)-
374 biotin (#029-08713, WAKO). The fly strains used in this study are listed in Table EV2.
375 Genotypes corresponding to each figure are shown in Table EV3.

376

377 ***Intrinsically disordered region prediction***

378 Amino acid sequences were obtained from the FlyBase database [https://flybase.org/].
379 Disordered regions were predicted using the PSIPRED protein sequence analysis workbench in
380 DISOPRED3 [http://bioinf.cs.ucl.ac.uk/psipred/].

381

382 ***Adult wings and eyes phenotypes scoring***

383 Adult female flies were anesthetized using CO_2. The wing and eye images were acquired using
384 a Leica MZ16F fluorescent stereomicroscope (Leica Microsystems) equipped with a Leica
385 DFC450 C CCD camera. Each wing was manually classified into one of four categories: *Intact*
386 (no defect), *Mild* (≧50% of wing area intact), *Severe* (<50% but ≧5% of wing area intact), and
387 *Wingless* (<5% of wing area intact).

388

389 ***Molecular cloning***

390 For *pAc5-Caspases-myc-mNeonGreen*, the coding sequences of *Dcp-1* and *Drice* were
391 amplified using PCR from the corresponding *pUASz-Caspase::V5::TurboID* plasmids
392 (Muramoto *et al*, 2025). The coding sequence of myc-tagged mNeonGreen was PCR-amplified
393 from *pUASz-Drice::myc::mNeonGreen plasmid* (Muramoto *et al*, 2025). The two fragments

394 were ligated into EcoRI/XhoI-digested *pAc5_STABLE2_neo* (González *et al*, 2011) using In-
395 Fusion (TaKaRa, Z9648N).

396 For *pCold I-EcoRI-CCT8-EcoRI*, the coding sequence of *CCT8* was PCR-amplified
397 from *Drosophila* cDNA, and the fragment was ligated into the *Eco*RI-digested *pCold I DNA*
398 vector (#3361, TaKaRa) using In-Fusion.

399 For *pAc5-Caspases^{CG}-myc*, the coding sequences of *Dcp-1* and *Drice* were PCR
400 amplified from the corresponding *pAc5-Caspases-myc-mNeonGreen* plasmids. The fragments
401 were ligated into EcoRI/BamHI-digested *pAc5_STABLE2_neo* (González *et al*, 2011) using In-
402 Fusion. For pAct-Bruce$^{1\text{-}900a}$a-3xFLAG, the first 900 aa of the coding sequences of *Bruce* were
403 PCR-amplified from *Drosophila* cDNA, and the fragment was ligated into the *Eco*RI-digested
404 *pAc5-Fasciclin 3 isoform A-3xFLAG* plasmids (Muramoto *et al*, 2025) using In-Fusion. For
405 *pAc5-3xFLAG-mRuby*3, *Drosophila* codon-optimized mRuby3 was synthesized (Integrated
406 DNA Technologies, Coralville, IA, USA) and ligated into the BamHI-digested *pAc5-3xFLAG-*
407 *Bub3* plasmids (Shinoda *et al*, 2023) using In-Fusion.

408 For mStayGold::C4 linker::V5-tag knock-in for Bruce, the guide RNA was identified
409 using the CRISPR Optimal Target Finder tool available on flyCRISPR
410 [http://flycrispr.molbio.wisc.edu/]. The DNA fragments for the guide RNA were subcloned into
411 BbsI-digested pDCC6 vectors (#59985, Addgene) (Gokcezade *et al*, 2014) to establish the
412 *pDCC6-dBruce-sgRNA* plasmid. The following primers were annealed to generate the DNA
413 fragments for guide RNAs: 5′-CTTCGCTTGCTTGAGGACGCGCTGC-3′ and 5′-
414 AAACGCAGCGCGTCCTCAAGCAAGC-3′. For the generation of the homology-directed
415 repair template (*pBac-mStayGold-c4-V5-dBruce-donor-3xP3-dsRed-polyA*), DNA fragments
416 of the 5′ homology arm were assembled into the BsaI site, and the DNA fragment of the 3′
417 homology arm with mStayGold::C4 linker::V5-tag was assembled into the SapI site of
418 pBac[3xP3-DsRed_polyA_Scarless_TK] (Shinoda *et al*, 2019) using In-Fusion. The PAM

419 sequence (TGG) of the gRNA-binding sites in the donor template was mutated (TGA) to
420 prevent Cas9-directed cleavage following homology-directed repair. The mStayGold::C4
421 linker::V5-tag fragment was amplified from pRSETB/mStayGold(c4) (#212018; Addgene)
422 (Ando *et al*, 2024) with V5-tag harboring primers. DNA fragments were amplified using PCR
423 with the following primers: dBruce 5′ homology arm (forward primer, 5′-
424 TGAAGGTCTCCTTAAAAGCCCGATTGGCGGCGCAGGAAGT-3′, and reverse primer,
425 5′-TCTTTCTAGGGTTAATCGAGTGCCCAGGGGGCGCGCGAGT-3′), dBruce 3′
426 homology arm-1 (forward primer, 5′-
427 TCTTTCTAGGGTTAATTTTTGGCATTCACAGGCGATTGCT-3′, and reverse primer, 5′-
428 TCCGGAGGTGCGCCGCGGCAATTTG-3′), mStayGold-C4 linker-V5-tag (forward primer,
429 5′-CGGCGCACCTCCGGAATGGTGTCTACAGGCGAGGAGCTGT-3′, and reverse primer,
430 5′-
431 GGTGCTGTCCAGGCCCAGCAGGGGGTTGGGGATGGGCTTGCCCACGGCAGAAGC
432 AGAAGGCTCGTGC-3′), 3′ homology arm-2 with mutated PAM (forward primer, 5′-
433 GGCCTGGACAGCACCGCCACGGAGCAGCATCATCAGCAGCGCGTCCTCAA-3′, and
434 reverse primer, 5′-GACGGCTCTTCATTAACTCTTAAATCAAATTTAAATTGAA-3′). The
435 established plasmids were injected into *yw; nos-Cas9(II-attP40)* for CRISPR/Cas9-mediated
436 transgenesis (BestGene Inc.). Each DsRed-positive transformant was isogenized and confirmed
437 using genomic PCR and sequencing.
438 All established plasmids were sequenced by Eurofins, Inc. The detailed plasmid DNA
439 sequences are available upon request.
440
441 ***Cell culture***

442 *Drosophila* S2 cells were grown at 25°C in Schneider's *Drosophila* medium (GIBCO,
443 21720001) supplemented with 10% (v/v) heat-inactivated fetal bovine serum, 100 U/mL
444 penicillin, and 100 μg/mL streptomycin (WAKO, 168-23191).
445
446 ***mNeonGreen signal quantification of S2 cells***
447 *Drosophila* S2 cells (2.5×10^5) seeded in 24-well plates were transfected with 200 ng of the
448 desired plasmid using Effectene Transfection Reagent (QIAGEN, 301427) following the
449 manufacturer's protocol. Sixteen hours after transfection, cells were transferred to four-
450 compartment glass-bottomed dishes (Greiner #627870). After another 24 hours, images were
451 captured using a Leica TCS SP8 confocal microscope (Leica Microsystems).
452 The mNeon Green intensity was quantified using Fiji (ImageJ) software (NIH Image).
453 Images were analyzed automatically using the ImageJ macro, as previously described (Fujisawa
454 *et al*, 2020) with modifications. Briefly, the mNeonGreen channel was filtered by the "Gaussian
455 Blur (sigma = 1)", processed with "Auto Threshold ("Mean" method)," processed with
456 "Watershed," and processed with "Analyze particles (size = 40–200 μm^2, circularity = 0.2–1.0)"
457 to define the region of interest. For a given region of interest, the average mNeon Green
458 intensity was measured.
459
460 ***Protein preparation of Drosophila tissues***
461 Whole larvae without digestive tract and fatobodies, larval salivary glands, fatbodies, brains,
462 wing discs and whole adults, adult thoraxes, ovaries, and testises of desired genotype were
463 dissected and lysed with RIPAi buffer (50 mM Tris-HCl, pH 8.0, 150 mM sodium chloride, 0.5
464 wt/vol% sodium deoxycholate, 0.1% w/v sodium dodecyl sulfate, and 1.0% w/v NP-40)
465 supplemented with cOmplete ULTRA EDTA-free protease inhibitor cocktail (#05892953001,
466 Roche). Samples were homogenized and centrifuged at 20,000 × *g*, 4°C for 10 min. The

467 supernatants were collected and snap-frozen in liquid nitrogen. Protein concentrations were
468 determined using the BCA assay (#297-73101, Wako) following the manufacturer's protocol.
469 The samples were mixed with Laemmli buffer, boiled at 95°C for 5 min, and then subjected to
470 western blotting analysis.
471
472 ***Western blotting***
473 Each sample was separated using SDS-PAGE. The proteins were then transferred onto
474 Immobilon-P polyvinylidene fluoride membranes (#IPVH00010; Millipore) for
475 immunoblotting. Membranes were blocked with 4% skim milk diluted in 1× TBST.
476 Immunoblotting was performed using the antibodies mentioned below, which were diluted with
477 4% skim milk. Signals were visualized using Immobilon Western Chemiluminescent HRP
478 Substrate (#WBKLS0500; Millipore) and FUSION SOLO. 7S. EDGE (Vilber-Lourmat).
479 Contrast and brightness adjustments were applied equally using Fiji (ImageJ) software (NIH
480 Image).
481 The primary antibodies used included mouse anti-V5 monoclonal antibody (1:1,000,
482 #46-0705, Invitrogen), mouse anti-FLAG M2 monoclonal antibody (1:5,000, Sigma), rabbit
483 anti-CCT8 polyclonal antibody (1:5,000, this study), rabbit anti-Myc-Tag (71D10) monoclonal
484 antibody (1:5,000, #2278, CST), rabbit anti-3xDYKDDDDK Tag (3xFLAG Tag) (E7C5T)
485 monoclonal antibody (1:5,000, #87537, CST), mouse anti-alpha tubulin (DM1A) monoclonal
486 antibody (1:10,000, #T9026, Sigma), mouse anti-Histone H3 (1B1B2) monoclonal antibody
487 (1:10,000, #14269, CST), and mouse anti-Actin monoclonal antibody (1:5,000; #A4700,
488 Sigma). The secondary antibodies used were goat anti-rabbit IgG horseradish peroxidase
489 (HRP)-conjugated antibody (1:5,000, #7074S, CST) and goat/rabbit/donkey anti-mouse IgG
490 HRP Conjugate (1:5,000, #W402B, Promega). The membranes for streptavidin blotting were

491 blocked with 3% bovine serum albumin. Streptavidin blotting was performed using
492 streptavidin-HRP (1:10,000, #SA10001; Invitrogen) diluted in 3% bovine serum albumin.
493
494 ***Experimental design for liquid chromatography–mass spectrometry (LC-MS/MS) analyses***
495 Two biological replicates were analyzed for each experimental condition to determine the
496 abundance of Drice/Dcp-1::TurboID relative to the control.
497
498 ***Purification of biotinylated proteins***
499 Samples were prepared as previously described (Shinoda *et al*, 2023). Briefly, 100 μg of
500 biotinylated protein-containing lysate was subjected to FG-NeutrAvidin bead (#TAS8848
501 N1171, Tamagawa Seiki) purification. FG-NeutrAvidin beads (25 μL, approximately 500 μg)
502 were washed three times with RIPA buffer. Benzonase-treated biotinylated protein samples
503 suspended in 1 mL of RIPA buffer were incubated overnight at 4°C. Conjugated beads were
504 magnetically isolated and washed with 500 μL of an ice-cold RIPA buffer solution, 1 M KCl
505 solution, 0.1 M Na_2CO_3 solution, and 4 M urea solution. For western blot analyses, the purified
506 samples were mixed with Laemmli buffer, boiled at 95°C for 5 min, and then subjected to
507 western blot analysis. For LC-MS/MS analysis, the purified samples were washed with 500 μL
508 ultrapure water (#214-01301, Wako) and 500 μL of 50 mM ammonium bicarbonate. The
509 samples were then mixed with 50 μL of 0.1% Rapigest diluted in 50 mM ammonium
510 bicarbonate, and 5 μL of 50 mM TCEP was subsequently added. Samples were incubated at
511 60°C for 5 min, and then 2.5 μL of 200 mM methyl methanethiosulfonate was added. One
512 microgram sequence-grade modified trypsin (#V5111, Promega) was then added for on-bead
513 trypsin digestion at 37°C, leaving the treatment for 16 h. The beads were then magnetically
514 isolated, and 60 μL of the supernatant was collected. Then, 3 μL of 10% trifluoroacetic acid
515 was added to the supernatants, incubating them at 37°C for 60 min with gentle agitation. The

516 samples were then centrifuged at 20,000 × *g*, 4°C for 10 min. The peptides were then
517 desalinated and purified using a GL-tip SDB (#7820-11200, GL Sciences) following the
518 manufacturer's instructions. The samples were speed-backed at 45°C for 30 min and dissolved
519 in 25 µL of 0.1% formic acid. The samples were then centrifuged at 20,000 × *g*, 4°C for 10
520 min, and the supernatants were collected. The peptide concentrations were determined using
521 the BCA assay. Finally, 500 ng of the purified protein was subjected to LC-MS/MS analysis.
522
523 ***LC-MS/MS analyses***
524 Samples were loaded onto an Acclaim PepMap 100 C18 column (75 µm x 2 cm, 3 µm particle
525 size and 100 Å pore size; #164946, Thermo Fisher Scientific) and separated on a nano-capillary
526 C18 column, (75 µm x 12.5 cm, 3 µm particle size, #NTCC-360/75-3-125, Nikkyo Technos)
527 using EASY-nLC 1200 system (Thermo Fisher Scientific). Elution conditions are listed in
528 Table EV4. The separated peptides were analyzed using QExactive (Thermo Fisher Scientific)
529 in data-dependent MS/MS mode. The parameters for the MS/MS analysis are listed in Table
530 EV5. The collected data were analyzed using Proteome Discoverer (PD) 2.2 software with the
531 Sequest HT search engine. The parameters for the PD 2.2 analysis are described in Table EV6.
532 Peptides were filtered at a false discovery rate of 0.01 using the Percolator node. Label-free
533 quantification was performed based on the intensities of the precursor ions using a precursor-
534 ion quantifier node. Normalization was performed using the total amount of peptides in all
535 average scaling modes. MS proteomic data were deposited in the ProteomeXchange
536 Consortium via the jPOST partner repository with the dataset identifier PXD067425 (Okuda *et*
537 *al*, 2017).
538
539 ***Anti-CCT8 antibody generation***

540 CCT8 was expressed in *Escherichia coli BL21* transformed with *pCold I-EcoRI-CCT8-EcoRI*.
541 Cells were grown at 37 °C overnight, diluted to OD_{600} 0.2 and cultured until OD_{600} 0.5 at 37°C.
542 Protein expression was induced by the addition of 1 mM IPTG at 15°C for 24 h. Cells were
543 centrifuged at 4000 × *g*, 4 °C for 20 min and resuspended in phosphate-buffered saline (PBS).
544 Cells were centrifuged at 4000 × *g*, 4°C for 10 min. Purification of 6x His-tagged CCT8 was
545 performed using the QIAexpress Ni-NTA Fast Start Kit (#30600, Qiagen) according to the
546 manufacturer's protocol: purification of 6xHis-tagged proteins under denaturing conditions.
547 Briefly, the cell pellets were lysed in Lysis Buffer (Denaturing Buffer adjusted to pH 8.0) with
548 gentle agitation for 60 min. The sample was centrifuged at 9,200 × *g*, 20°C for 30 min. The
549 supernatant was applied to Fast Start column and washed twice with Wash Buffer (Denaturing
550 Buffer adjusted to pH 6.3). Proteins were eluted using Elution Buffer (Denaturing Buffer
551 adjusted to pH 4.5). Polyclonal antibodies were raised in rabbits using purified 6xHis-tagged
552 CCT8 as an immunogen (Eurofins Inc.).
553
554 ***Protein complexes prediction with AlphaFold3***
555 Amino acid sequences were obtained from the FlyBase database [https://flybase.org/]. The
556 protein complex structures were predicted using AlphaFold3 (Abramson *et al*, 2024) on the
557 AlphaFold server [https://alphafoldserver.com/].
558
559 ***Co-immunoprecipitation***
560 *Drosophila* S2 cells (2.0×10^6) seeded in 6-well plates were transfected with the desired
561 plasmid using Effectene Transfection Reagent. For live cell lysate, *Drosophila* S2 cells were
562 lysed on ice using 550 µL of IP lysis buffer (50 mM Tris-HCl (pH 7.5), 150 mM NaCl, 0.5%
563 NP-40) supplemented with cOmplete ULTRA EDTA-free protease inhibitor cocktail. For
564 apoptotic cell lysate, the cells were treated with 10 µg/mL cycloheximide (#C7698, Sigma) for

565 apoptosis induction. After 6 h of incubation, cells were harvested and centrifuged at 800 × *g*,
566 4 °C for 5 min and washed twice. Then, cells were lysed by using 550 μL of IP lysis buffer (50
567 mM Tris-HCl (pH 7.5), 150 mM NaCl, and 0.5% NP-40) supplemented with cOmplete
568 ULTRA EDTA-free protease inhibitor cocktail. The cell lysates were centrifuged at 20,000 × *g*,
569 4 °C for 5 min. Supernatants (50 μL) were collected as inputs. The remainder of the supernatant
570 was incubated for 2 h at 4°C with 20 μL of anti-DDDDK-tag mAb-Magnetic Agarose (#M185-
571 10R, MBL) equilibrated with the IP lysis buffer. The beads were washed thrice in IP lysis buffer
572 and boiled for 5 min at 95°C with 50 μL 1× Laemmli buffer. The samples were magnetically
573 separated, and the supernatants were subjected to SDS-PAGE.
574
575 ***Immunohistochemistry***
576 Wing imaginal discs of the late third-instar larvae and testes and ovaries of the adults were fixed
577 with 4% paraformaldehyde in PBS. The wing imaginal discs and testes samples were washed
578 in PBS containing 0.1% Triton X-100 (PBST), and the ovary samples were washed in 1.0%
579 PBST, blocked in PBST with 5% normal donkey serum (PBSTn) for 30 min, and incubated
580 with primary antibodies in PBSTn overnight at 4°C. The samples were washed with PBST,
581 incubated for 2 h with secondary antibodies suspended in PBSTn, and washed again with PBST.
582 Images were captured using a TCS SP8 microscope (Leica Microsystems).
583 The primary antibodies used were mouse anti-Myc-tag monoclonal antibody (1:500,
584 #R950-25, Invitrogen) and mouse anti-V5 tag monoclonal antibody (1:100, #960-25,
585 Invitrogen). The secondary antibodies used were Alexa488-conjugated donkey anti-mouse IgG
586 (1:500 (Myc) or 1:100 (V5), #A-21202, Thermo Fisher Scientific). Hoechst 33342 (8 μM;
587 #H3570, Invitrogen) for nuclear staining was used during the secondary antibody incubation.
588 Images were analyzed and edited using ImageJ software.
589

590 ***Wing size measurement***

591 Flies were raised, and their wings were mounted and digitized as previously described (Shinoda
592 *et al*, 2019). Briefly, flies were placed on an acetic acid agar plate (2% agar, 1% sucrose, and
593 0.36% acetic acid) to lay eggs overnight. The plates were collected, and the eggs were incubated
594 at 25°C for 24 h. The 1st instar larvae were collected from the agar plate, and 30 larvae were
595 placed in one vial to precisely control the larval density. These flies were raised at 25°C. After
596 more than two days of hatching, the adult female flies were collected and submerged in 99.5%
597 ethanol to dehydrate for 24 hours. Dehydrated flies were dissected to mount their wings using
598 Euparal (Waldeck) with the dorsal side upward. Images were digitized using an upright
599 microscope (Leica DM5000B; Leica Microsystems) equipped with a CCD camera. The wing
600 size was measured using a Drosophila wing digital twin
601 [https://datamarkin.com/models/drosophila-wings-beta] developed by Datamarkin. Areas 0, 1,
602 and 2 were quantified as the anterior parts, whereas areas 4, 6, 7, and 8 were quantified as the
603 posterior parts, respectively.

604

605 ***Statistical analysis***

606 The data are presented as the means ± standard error of measurement (SEM). *p*-values were
607 calculated using a one-way analysis of variance (ANOVA), followed by Sidak's multiple
608 comparison test for selected pairs (Fig. EV1B, C, D; Fig. 5K), or Dunnett's multiple comparison
609 test using GraphPad Prism 8. NS: $p \geqq 0.05$, †: $p < 0.05$.

610

611 **Acknowledgments**

612 We would like to thank G. W. Davis, R. Carthew, B. Hay, C-H. Cheng, H. Richardson, S. K.
613 Yoo, H. Steller, Y. Hiromi, H. D. Ryoo, the FlyORF Zurich ORFeome Project, Bloomington
614 *Drosophila* Stock Center, Vienna Drosophila Resource Center, Kyoto Stock Center, and NIG-
615 FLY for providing the fly strains. We thank Datamarkin for providing the Drosophila wing
616 digital twin tool. We thank Dr. S. Hirayama, Dr. S. Murata, and the One-Stop Sharing Faculty
617 Center for Future Drug Discovery at the Graduate School of Pharmaceutical Sciences,
618 University of Tokyo, for the LC-MS/MS analysis. We thank Miura's lab members for their
619 technical assistance and discussions; in particular, K. Takenaga for preparing the fly food and
620 R. Takamoto for experimental support. We thank *Editage* [www.editage.com] for the English
621 language editing of this manuscript. This work was supported by grants from the Ministry of
622 Education, Culture, Sports, Science, and Technology of Japan (KAKENHI Grant Numbers
623 19K16137, 21K15080, 22H05586, and 23K05747 to N.S. and 21H04774, 23H04766,
624 24H00567, and 25H01842 to M.M.), the Japan Agency for Medical Research and Development
625 (AMED; Grant number JP21gm5010001 to M.M.), and grants from the Takeda Science
626 Foundation and Sumitomo Foundation to N.S.

627

628 **Author Contributions**

629 N.S. and M.M. designed the study; N.S. conducted most of the experiments and analyzed most
630 of the data; Y.H conducted protein structural predictions; N.H. analyzed the expression patterns
631 of Drosophila caspases; and N.S. and M.M. wrote the manuscript.

632

633 **Conflict of Interest**

634 The authors declare that they have no conflict of interest.

635

636 **References**

637 Abramson J, Adler J, Dunger J, Evans R, Green T, Pritzel A, Ronneberger O, Willmore L,
638 Ballard AJ, Bambrick J, *et al* (2024) Accurate structure prediction of biomolecular
639 interactions with AlphaFold 3. *Nature* 630: 493–500

640 Ando R, Shimozono S, Ago H, Takagi M, Sugiyama M, Kurokawa H, Hirano M, Niino Y,
641 Ueno G, Ishidate F, *et al* (2024) StayGold variants for molecular fusion and membrane-
642 targeting applications. *Nat Methods* 21: 648–656

643 Aram L, Yacobi-Sharon K & Arama E (2017) CDPs: caspase-dependent non-lethal cellular
644 processes. *Cell Death Differ* 24: 1307–1310

645 Arama E, Agapite J & Steller H (2003) Caspase activity and a specific cytochrome C are
646 required for sperm differentiation in Drosophila. *Dev Cell* 4: 687–697

647 Arama E, Bader M, Rieckhof GE & Steller H (2007) A ubiquitin ligase complex regulates
648 caspase activation during sperm differentiation in Drosophila. *PLoS Biol* 5: e251

649 Berthelet J & Dubrez L (2013) Regulation of apoptosis by inhibitors of apoptosis (IAPs). *Cells*
650 2: 163–187

651 Boucher D, Blais V & Denault J-B (2012) Caspase-7 uses an exosite to promote poly(ADP
652 ribose) polymerase 1 proteolysis. *Proc Natl Acad Sci U S A* 109: 5669–5674

653 Branon TC, Bosch JA, Sanchez AD, Udeshi ND, Svinkina T, Carr SA, Feldman JL, Perrimon
654 N & Ting AY (2018) Efficient proximity labeling in living cells and organisms with
655 TurboID. *Nat Biotechnol* 36: 880–887

656 Choutka C, DeVorkin L, Go NE, Hou Y-CC, Moradian A, Morin GB & Gorski SM (2017)
657 Hsp83 loss suppresses proteasomal activity resulting in an upregulation of caspase-
658 dependent compensatory autophagy. *Autophagy* 13: 1573–1589

659 Desroches A & Denault J-B (2019) Caspase-7 uses RNA to enhance proteolysis of poly(ADP-
660 ribose) polymerase 1 and other RNA-binding proteins. *Proc Natl Acad Sci U S A* 116:
661 21521–21528

662 DeVorkin L, Go NE, Hou Y-CC, Moradian A, Morin GB & Gorski SM (2014) The Drosophila
663 effector caspase Dcp-1 regulates mitochondrial dynamics and autophagic flux via SesB.
664 *J Cell Biol* 205: 477–492

665 Dietz L, Ellison CJ, Riechmann C, Cassidy CK, Felfoldi FD, Pinto-Fernández A, Kessler BM
666 & Elliott PR (2023) Structural basis for SMAC-mediated antagonism of caspase
667 inhibition by the giant ubiquitin ligase BIRC6. *Science* 379: 1112–1117

668 Ditzel M, Broemer M, Tenev T, Bolduc C, Lee TV, Rigbolt KTG, Elliott R, Zvelebil M,
669 Blagoev B, Bergmann A, *et al* (2008) Inactivation of effector caspases through
670 nondegradative polyubiquitylation. *Mol Cell* 32: 540–553

671 Domingues C & Ryoo HD (2012) Drosophila BRUCE inhibits apoptosis through non-lysine
672 ubiquitination of the IAP-antagonist REAPER. *Cell Death Differ* 19: 470–477

673 Ehrmann JF, Grabarczyk DB, Heinke M, Deszcz L, Kurzbauer R, Hudecz O, Shulkina A,
674 Gogova R, Meinhart A, Versteeg GA, *et al* (2023) Structural basis for regulation of
675 apoptosis and autophagy by the BIRC6/SMAC complex. *Science* 379: 1117–1123

676 Florentin A & Arama E (2012) Caspase levels and execution efficiencies determine the
677 apoptotic potential of the cell. *J Cell Biol* 196: 513–527

678 Fujisawa Y, Shinoda N, Chihara T & Miura M (2020) ROS Regulate Caspase-Dependent Cell
679 Delamination without Apoptosis in the Drosophila Pupal Notum. *iScience* 23: 101413

680 Furuyama T, Banerjee R, Breen TR & Harte PJ (2004) SIR2 is required for polycomb silencing
681 and is associated with an E(Z) histone methyltransferase complex. *Curr Biol* 14: 1812–
682 1821

683 Gokcezade J, Sienski G & Duchek P (2014) Efficient CRISPR/Cas9 plasmids for rapid and
684 versatile genome editing in Drosophila. *G3 (Bethesda)* 4: 2279–2282

685 González M, Martín-Ruíz I, Jiménez S, Pirone L, Barrio R & Sutherland JD (2011) Generation
686 of stable Drosophila cell lines using multicistronic vectors. *Sci Rep* 1: 75

687 Haberman AS, Akbar MA, Ray S & Krämer H (2010) Drosophila acinus encodes a novel
688 regulator of endocytic and autophagic trafficking. *Development* 137: 2157–2166

689 Hou Y-CC, Chittaranjan S, Barbosa SG, McCall K & Gorski SM (2008) Effector caspase Dcp-
690 1 and IAP protein Bruce regulate starvation-induced autophagy during Drosophila
691 melanogaster oogenesis. *J Cell Biol* 182: 1127–1139

692 Hunkeler M, Jin CY & Fischer ES (2023) Structures of BIRC6-client complexes provide a
693 mechanism of SMAC-mediated release of caspases. *Science* 379: 1105–1111

694 Ikegawa Y, Combet C, Groussin M, Navratil V, Safar-Remali S, Shiota T, Aouacheria A &
695 Yoo SK (2023) Evidence for existence of an apoptosis-inducing BH3-only protein,
696 sayonara, in Drosophila. *EMBO J* 42: e110454

697 Jacomin A-C, Petridi S, Di Monaco M, Bhujabal Z, Jain A, Mulakkal NC, Palara A, Powell EL,
698 Chung B, Zampronio C, *et al* (2020) Regulation of Expression of Autophagy Genes by
699 Atg8a-Interacting Partners Sequoia, YL-1, and Sir2 in Drosophila. *Cell Rep* 31: 107695

700 Julien O & Wells JA (2017) Caspases and their substrates. *Cell Death Differ* 24: 1380–1389

701 Kaplan Y, Gibbs-Bar L, Kalifa Y, Feinstein-Rotkopf Y & Arama E (2010) Gradients of a
702 ubiquitin E3 ligase inhibitor and a caspase inhibitor determine differentiation or death
703 in spermatids. *Dev Cell* 19: 160–173

704 Kim Y-I, Ryu T, Lee J, Heo Y-S, Ahnn J, Lee S-J & Yoo O (2010) A genetic screen for
705 modifiers of Drosophila caspase Dcp-1 reveals caspase involvement in autophagy and
706 novel caspase-related genes. *BMC Cell Biol* 11: 9

707 Liu S-S, Jiang T-X, Bu F, Zhao J-L, Wang G-F, Yang G-H, Kong J-Y, Qie Y-F, Wen P, Fan
708 L-B, *et al* (2024) Molecular mechanisms underlying the BIRC6-mediated regulation of
709 apoptosis and autophagy. *Nat Commun* 15: 891

710 Muramoto M, Hanawa N, Okumura M, Chihara T, Miura M & Shinoda N (2025) Executioner
711 caspase is proximal to Fasciclin 3 which facilitates non-lethal activation in Drosophila
712 olfactory receptor neurons. *Elife* 13

713 Nakajima Y-I & Kuranaga E (2017) Caspase-dependent non-apoptotic processes in
714 development. *Cell Death Differ* 24: 1422–1430

715 Nandi N, Tyra LK, Stenesen D & Krämer H (2014) Acinus integrates AKT1 and subapoptotic
716 caspase activities to regulate basal autophagy. *J Cell Biol* 207: 253–268

717 Newman BL, Lundblad JR, Chen Y & Smolik SM (2002) A Drosophila homologue of Sir2
718 modifies position-effect variegation but does not affect life span. *Genetics* 162: 1675–
719 1685

720 Newton K, Strasser A, Kayagaki N & Dixit VM (2024) Cell death. *Cell* 187: 235–256

721 Nezis IP, Shravage BV, Sagona AP, Lamark T, Bjørkøy G, Johansen T, Rusten TE, Brech A,
722 Baehrecke EH & Stenmark H (2010) Autophagic degradation of dBruce controls DNA
723 fragmentation in nurse cells during late Drosophila melanogaster oogenesis. *J Cell Biol*
724 190: 523–531

725 Okuda S, Watanabe Y, Moriya Y, Kawano S, Yamamoto T, Matsumoto M, Takami T,
726 Kobayashi D, Araki N, Yoshizawa AC, *et al* (2017) jPOSTrepo: an international
727 standard data repository for proteomes. *Nucleic Acids Res* 45: D1107–D1111

728 Qin W, Cho KF, Cavanagh PE & Ting AY (2021) Deciphering molecular interactions by
729 proximity labeling. *Nat Methods* 18: 133–143

730 Shinoda N, Hanawa N, Chihara T, Koto A & Miura M (2019) Dronc-independent basal
731 executioner caspase activity sustains Drosophila imaginal tissue growth. *Proc Natl*
732 *Acad Sci U S A* 116: 20539–20544

733 Shinoda N, Horikoshi M, Taira Y, Muramoto M, Hirayama S, Murata S & Miura M (2023)
734 Caspase cleaves Drosophila BubR1 to modulate spindle assembly checkpoint function
735 and lifespan of the organism. *FEBS J* 290: 4200–4223

736 Shinoda N & Miura M (2024) Exploring caspase-dependent non-lethal cellular processes using
737 Drosophila. *Front Cell Death* 3: 1472108

738 Taira Y, Yang Z, Miyata Y, Shirasaki Y, Segawa K, Miura M & Shinoda N (2025) Early-
739 peaking caspase-7 activity at the plasma membrane drives apoptotic phosphatidylserine
740 exposure. *bioRxiv*: 2025.03.17.643603

741 Tyra LK, Nandi N, Tracy C & Krämer H (2020) Yorkie growth-promoting activity is limited
742 by Atg1-mediated phosphorylation. *Dev Cell* 52: 605-616.e7

743 Vaux DL & Silke J (2005) IAPs, RINGs and ubiquitylation. *Nat Rev Mol Cell Biol* 6: 287–297

744 Walsh JG, Cullen SP, Sheridan C, Lüthi AU, Gerner C & Martin SJ (2008) Executioner
745 caspase-3 and caspase-7 are functionally distinct proteases. *Proc Natl Acad Sci U S A*
746 105: 12815–12819

747 Wu G, Chai J, Suber TL, Wu JW, Du C, Wang X & Shi Y (2000) Structural basis of IAP
748 recognition by Smac/DIABLO. *Nature* 408: 1008–1012

749 Xie HB & Golic KG (2004) Gene deletions by ends-in targeting in Drosophila melanogaster.
750 *Genetics* 168: 1477–1489

751 Xu D, Li Y, Arcaro M, Lackey M & Bergmann A (2005) The CARD-carrying caspase Dronc
752 is essential for most, but not all,developmental cell death in*Drosophila*. *Development*
753 132: 2125–2134

754

755 **Figures and figure legends**

756 **Figure 1**

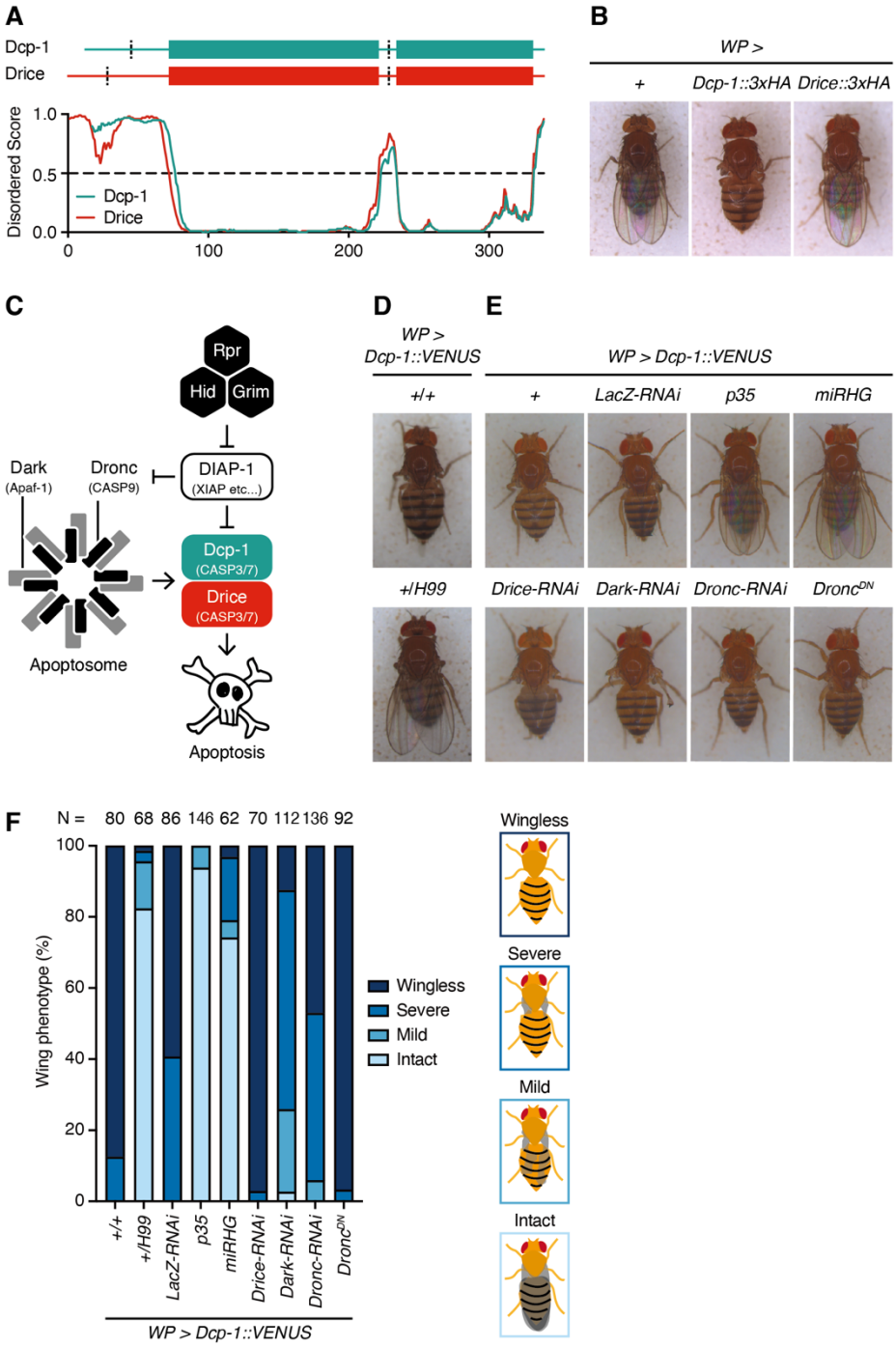

757

758 **Figure 1. *Dcp-1* overexpression induces apoptosis independent of the apoptosome.**

759 (A) Schematic structures and intrinsically disordered region prediction of Dcp-1 (dark cyan)
760 and Drice (red). The predicted disordered score plot is shown. Regions wherein the score is
761 more than 0.5 are predicted to be disordered.

762 (B) Representative images of female wing phenotypes upon caspase overexpression using *WP-*
763 *Gal4*.

764 (C) Schematic diagram of canonical apoptosis signaling in *Drosophila*.

765 (D, E) Representative images of female wing phenotypes upon *Dcp-1::VENUS* overexpression
766 using *WP-Gal4* with the genetic perturbation of canonical apoptosis signaling.
767 (F) Quantification of (D) and (E). Each wing is manually classified into four (wingless, severe,
768 mild, and intact) categories. Schematic images of the four categories are shown on the right.
769 Sample sizes are shown in the figure.
770

771 **Figure EV1**

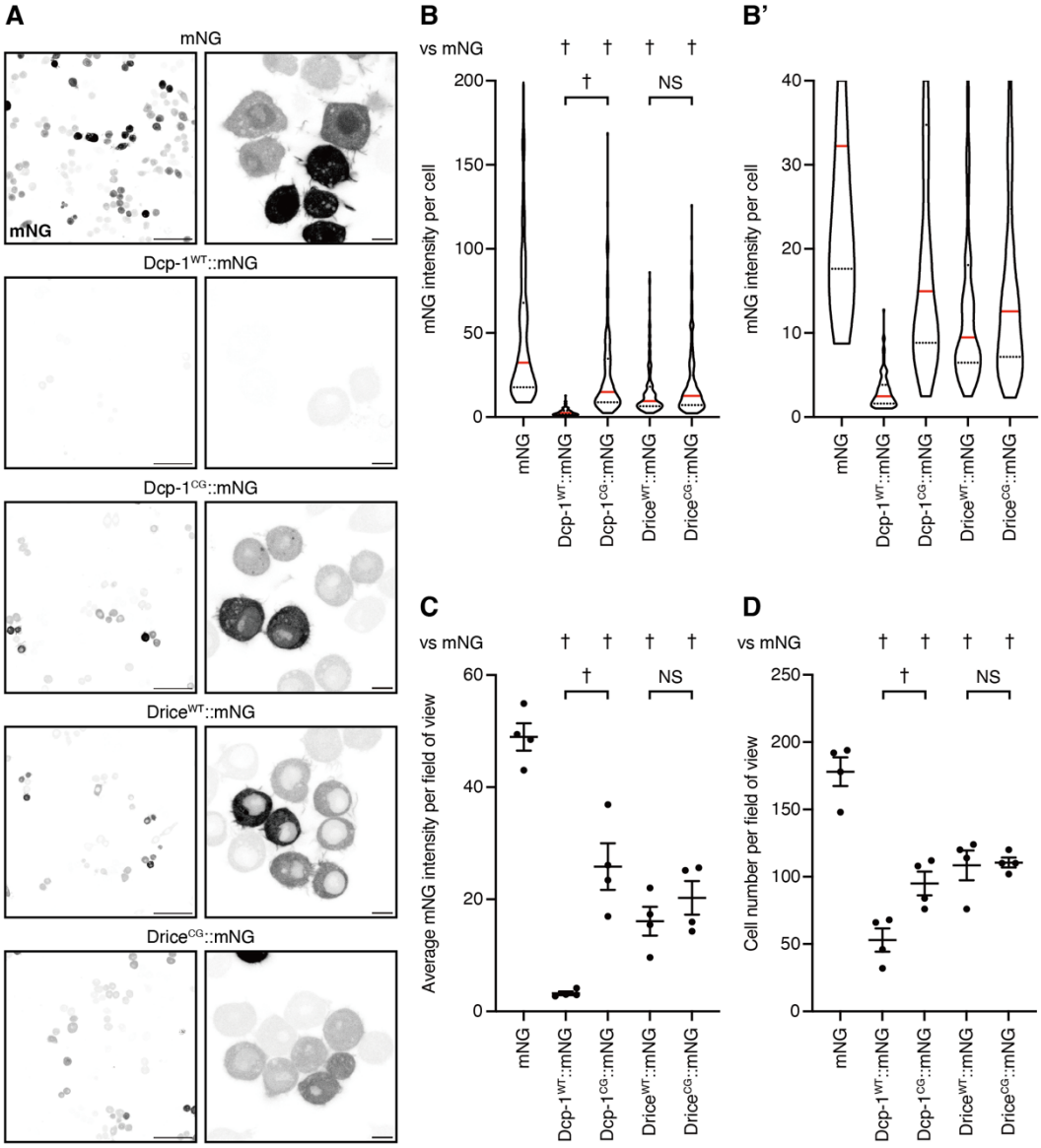

772

773 **Figure EV1. Dcp-1 overexpression induces apoptosis in *Drosophila* S2 cells.**
774 (A) Representative images of *Drosophila* S2 cells transfected with mNeonGreen (mNG)-tagged
775 wild-type (WT) or catalytically inactive (catalytic cysteine mutated to glycine; CG) Dcp-1 and
776 Drice. Scale bars: 50 µm (left) and 5 µm (right).
777 (B) Quantification of mNG intensity for each cell, shown as a violin plot. Quartiles are indicated
778 by black broken lines, and the median is indicated by a red bar. (B′) Magnified view of the data
779 in (B), with the Y-axis limited to 0–40. *p*-values were calculated using one-way analysis of
780 variance (ANOVA) followed by Sidak's multiple-comparison test for selected pairs. NS, $p >$
781 0.05; †, $p < 0.05$. Sample sizes: mNG (n = 712 cells), Dcp-1^{WT}::mNG (n = 212 cells), Dcp-
782 1^{CG}::mNG (n = 380 cells), $Drice^{WT}$::mNG (n = 434 cells), and $Drice^{CG}$::mNG (n = 442 cells).
783 (C) Quantification of the average mNG intensity in each field of view. Data are presented as
784 mean ± SEM. *p*-values were calculated using one-way ANOVA followed by Sidak's multiple-

785 comparison test for selected pairs. NS, $p \geqq 0.05$; †, $p < 0.05$. Sample size for each condition is
786 4.
787 (D) Quantification of the mNG-positive cell number in each field of view. Data are presented
788 as mean ± SEM. *p*-values were calculated using one-way ANOVA followed by Sidak's
789 multiple-comparison test for selected pairs. NS, $p \geqq 0.05$; †, $p < 0.05$. Sample size for each
790 condition is 4.
791

792 **Figure 2**

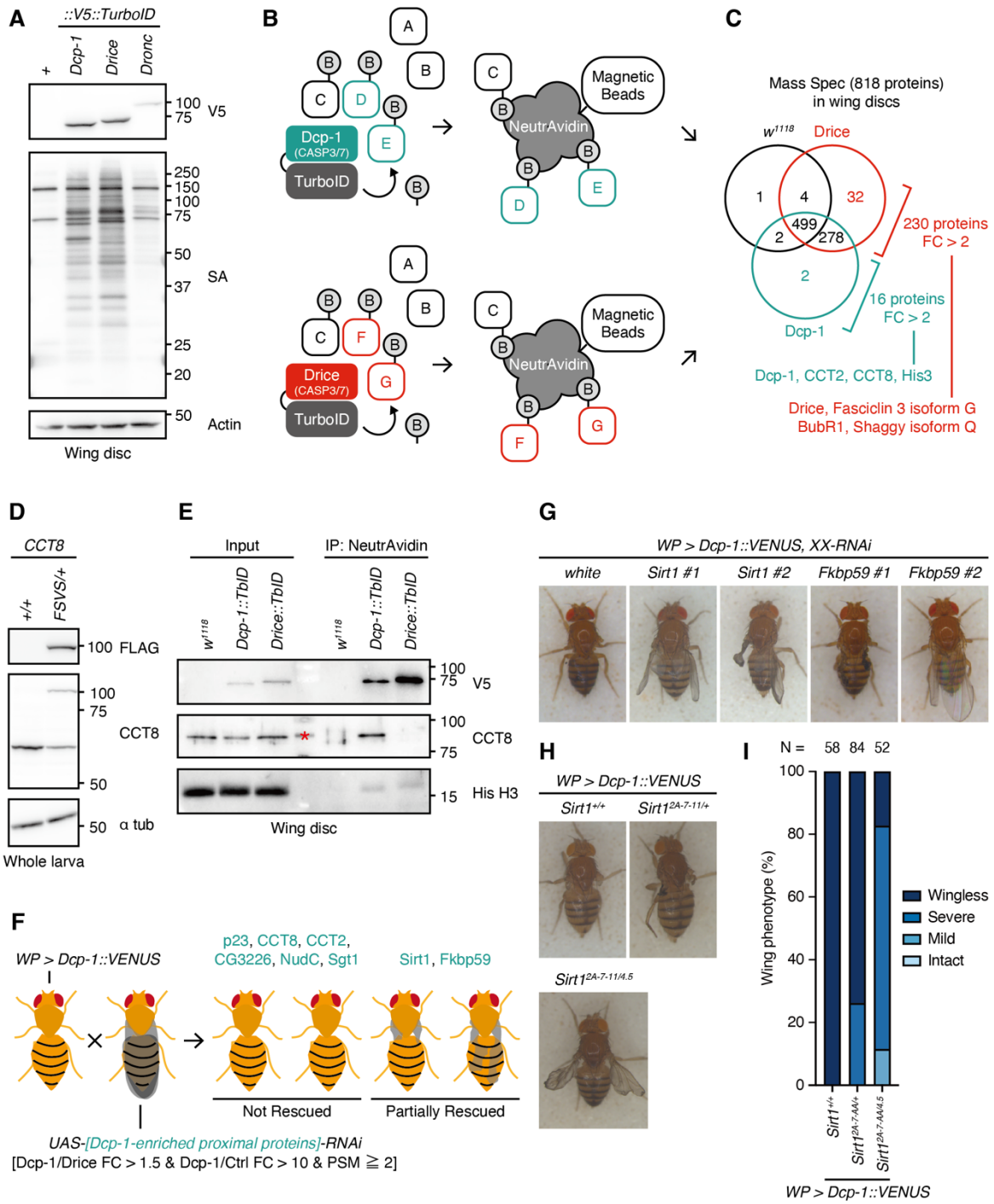

793

794 **Figure 2. Dcp-1-enriched proximal proteins are required for Dcp-1 activation.**
795 (A) Western blotting of expression of C-terminally V5::TurboID knocked-in tagged caspases
796 and biotinylation patterns of their proximal proteins detected by streptavidin (SA) in larval wing
797 imaginal discs.
798 (B) A schematic diagram of the TurboID-mediated identification of proximal proteins. Dcp-1-
799 and Drice-proximal proteins are promiscuously labeled in vivo with the administration of biotin.
800 Then, biotinylated proteins are purified using NeutrAvidin magnetic beads and are
801 subsequently analyzed by mass spectrometry.

802 (C) A summary of mass spectrometry analysis of proteins in the larval imaginal discs. Among
803 818 proteins identified, 230 proteins were detected as highly enriched proteins in
804 Drice::V5::TurboID flies (FC [Drice::V5::TurboID/Dcp-1::V5::TurboID] > 2) and 16 proteins
805 were detected as highly enriched proteins in Dcp-1::V5::TurboID flies flies (FC [Dcp-
806 1::V5::TurboID/Drice::V5::TurboID] > 2).
807 (D) Western blotting validation of the anti-CCT8 antibody in whole larval lysates without the
808 digestive tract and fat body. The anti-CCT8 antibody detects both endogenous CCT8 (MW:
809 59.4 kDa) and 3xFLAG::StrepII::VENUS::StrepII (FSVS)-tagged CCT8 (MW: 91.1 kDa).
810 (E) Western blotting of endogenous CCT8 expressed in larval wing imaginal disc. Dcp-1-
811 proximal and Drice-proximal proteins biotinylated by C-terminally knocked-in tagged
812 V5::TurboID are purified using NeutrAvidin. The red asterisk represents a non-specific band
813 in the marker lane.
814 (F) Schematic diagram of the RNAi screen targeting eight Dcp-1-enriched proximal proteins.
815 The *WP > Dcp-1::VENUS* line was crossed with each *UAS-RNAi* line, and wing phenotypes of
816 the F1 progeny were scored.
817 (G) Representative images of female wing phenotypes from *Dcp-1::VENUS* overexpression
818 driven by *WP-Gal4* with knockdown of Dcp-1-enriched proximal proteins. "XX" denotes the
819 knocked-down gene, and "#1" and "#2" indicate independent RNAi lines.
820 (H) Representative images of female wing phenotypes upon *Dcp-1::VENUS* overexpression
821 driven by *WP-Gal4* in the *Sirt1* null mutant background.
822 (I) Quantification of (H). Each wing is manually classified into four (wingless, severe, mild,
823 and intact) categories. Sample sizes are shown in the figure.
824

825 **Figure EV2**

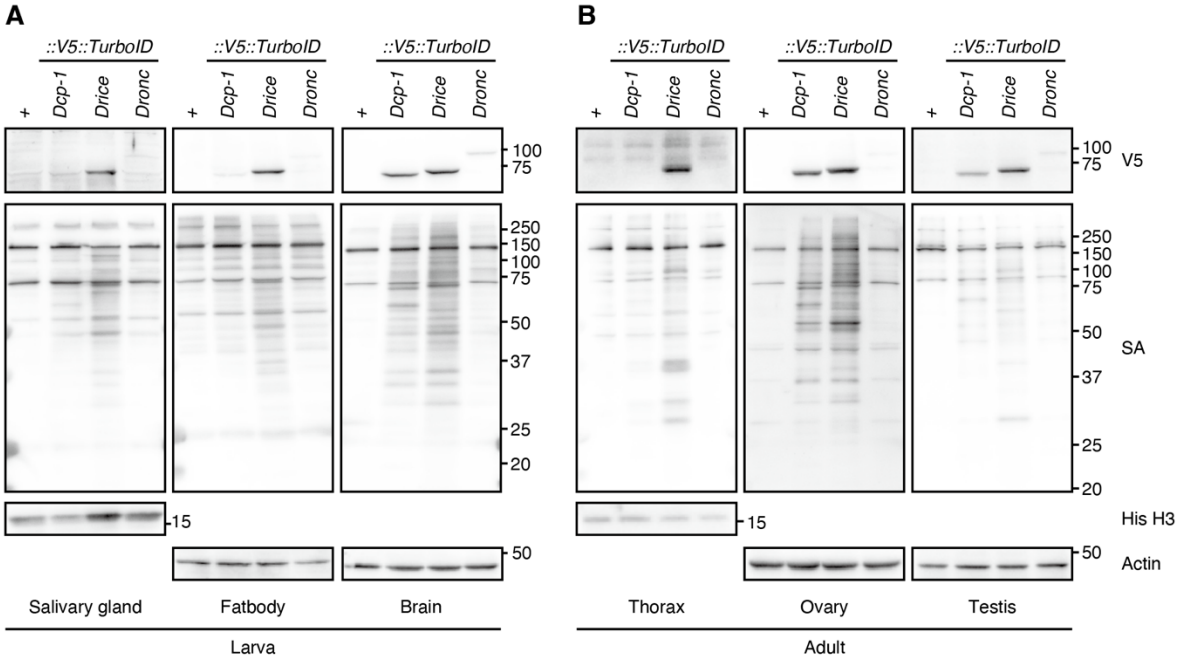

826

827 **Figure EV2. Expression patterns of *Drosophila* caspases in larval and adult tissues.**

828 (A) Western blotting of expression of C-terminally V5::TurboID knocked-in tagged caspases
829 and biotinylation patterns of their proximal proteins detected by streptavidin (SA) in larval
830 salivary gland, fat body, and brain.

831 (B) Western blotting of expression of C-terminally V5::TurboID knocked-in tagged caspases
832 and biotinylation patterns of their proximal proteins detected by SA in adult thorax, ovary, and
833 testis.

834

835 **Figure 3**

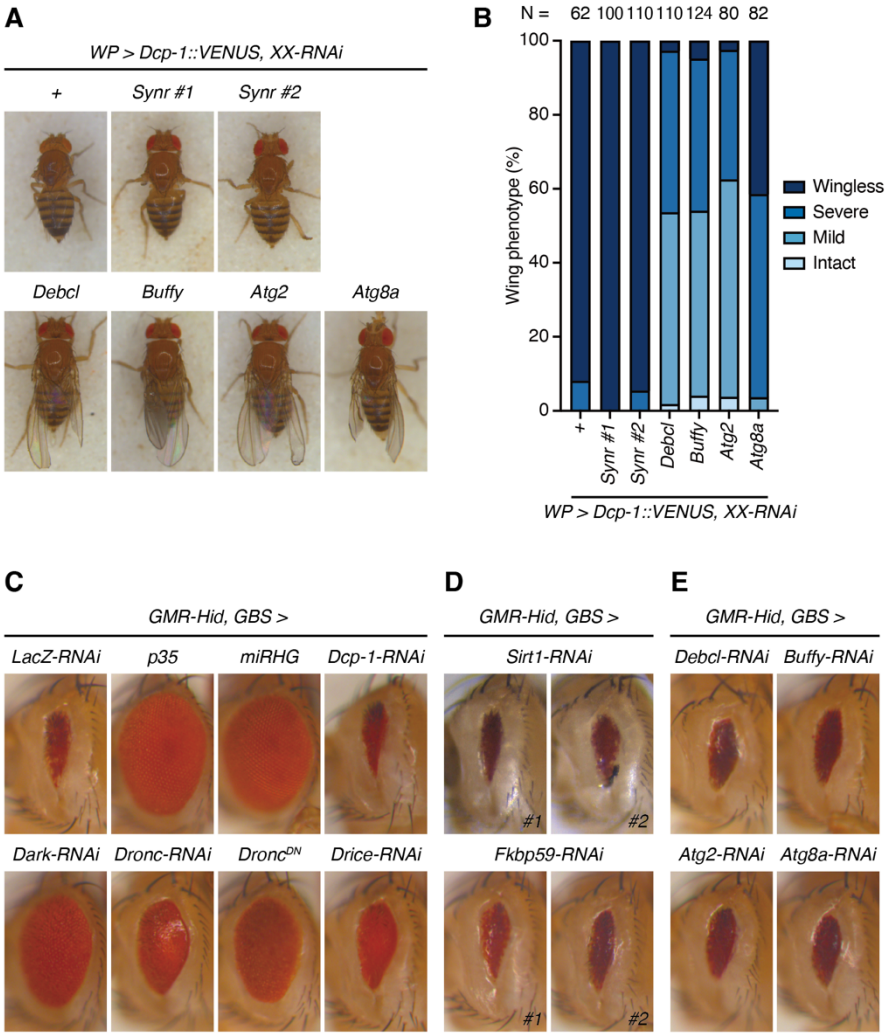

836

837 **Figure 3. Debcl, Buffy, and autophagy are specifically required for *Dcp-1* overexpression-**
838 **induced apoptosis.**

839 (A) Representative images of female wing phenotypes from *Dcp-1::VENUS* overexpression
840 driven by *WP-Gal4* with the genetic perturbation of *Synr*, *Debcl*, *Buffy,* and autophagy. "XX"
841 denotes the knocked-down gene, and "#1" and "#2" indicate independent RNAi lines.
842 (B) Quantification of (A). "XX" denotes the knocked-down gene, and "#1" and "#2" indicate
843 independent RNAi lines. Each wing is manually classified into four (wingless, severe, mild,
844 and intact) categories. Sample sizes are shown in the figure.
845 (C) Representative images of female eye phenotypes upon *Hid* overexpression with the genetic
846 perturbation of canonical apoptosis signaling.
847 (D) Representative images of female eye phenotypes upon *Hid* overexpression with the genetic
848 perturbation of *Sirt1* or *Fkbp59*. "#1" and "#2" indicate independent RNAi lines.
849 (E) Representative images of female eye phenotypes upon *Hid* overexpression with the genetic
850 perturbation of *Debcl*, *Buffy*, and autophagy.
851

852 **Figure EV3**

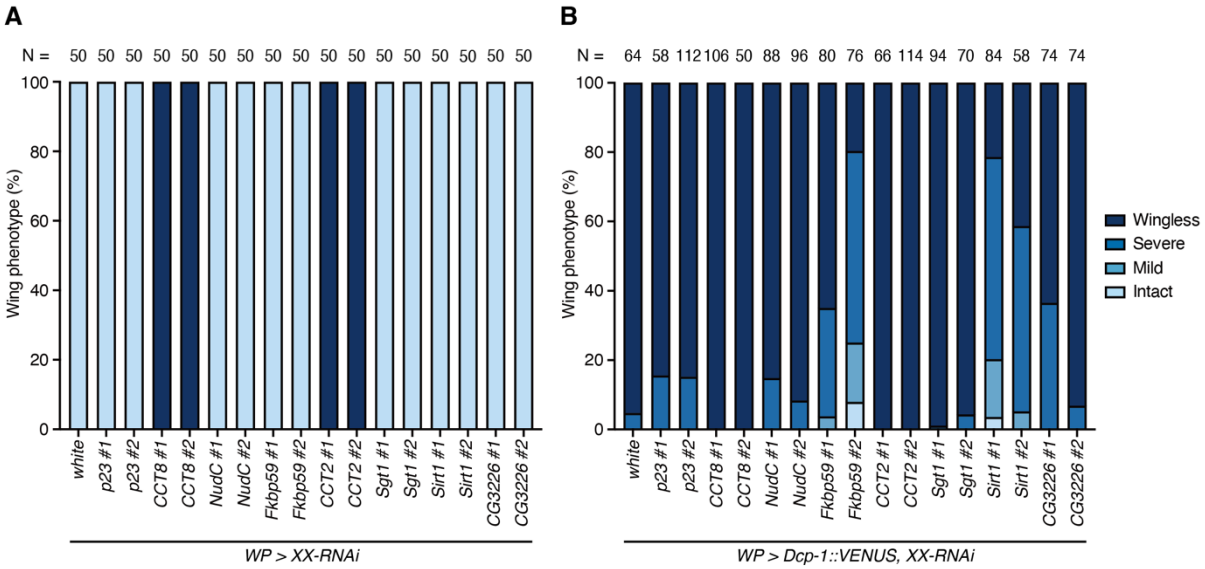

853

854 **Figure EV3. RNAi screening of Dcp-1-enriched proximal proteins for regulators of Dcp-**
855 **1 activation.**

856 (A) Quantification of female wing phenotypes upon knockdown of Dcp-1-enriched proximal
857 proteins driven by *WP-Gal4*. "XX" denotes the knocked-down gene, and "#1" and "#2" indicate
858 independent RNAi lines. Each wing is manually classified into four (wingless, severe, mild,
859 and intact) categories. Sample sizes are shown in the figure.

860 (B) Quantification of female wing phenotypes upon *Dcp-1::VENUS* overexpression driven by
861 *WP-Gal4* with simultaneous knockdown of Dcp-1-enriched proximal proteins. "XX" denotes
862 the knocked-down gene, and "#1" and "#2" indicate independent RNAi lines. Each wing is
863 manually classified into four (wingless, severe, mild, and intact) categories. Sample sizes are
864 shown in the figure.

865

866 **Figure 4**

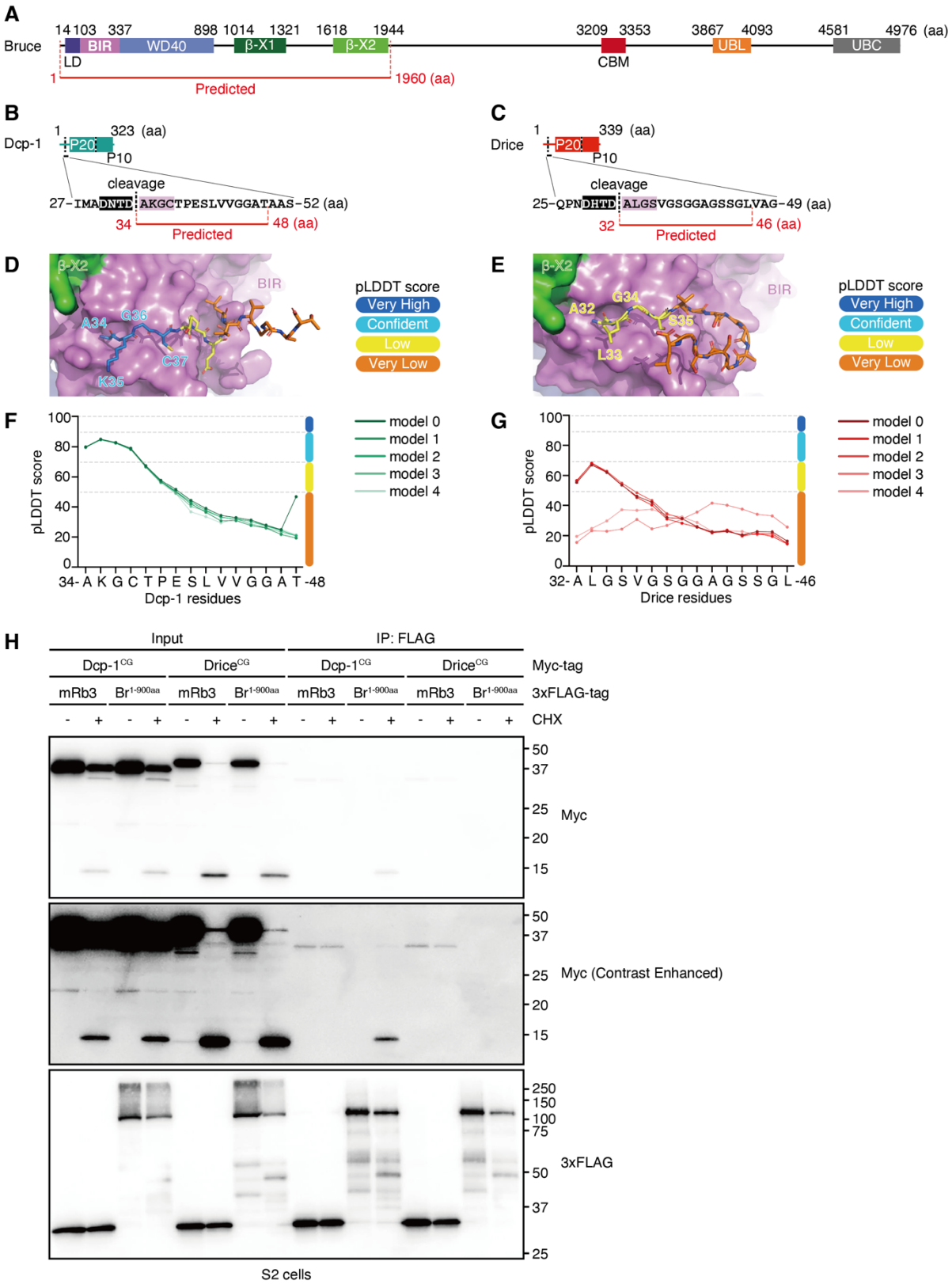

867

868 **Figure 4. Cleaved Dcp-1, but not Drice, interacts with Bruce.**

869 (A) Domain structure of Bruce. LD denotes the linker domain, WD40 a WD40 domain, BIR
870 the Baculoviral IAP repeat, β-X a β-sandwich-like fold, CBM a domain resembling the

carbohydrate-binding module family 32 (CBM), UBL the ubiquitin-like domain, and UBC the E2-E3 hybrid ubiquitin-conjugating (UBC) domain. The region used for structural prediction using AlphaFold3 is indicated in red.

(B) IBM-like sequence in Dcp-1. The propeptide cleavage site of Dcp-1 is indicated by a black dashed line; the caspase recognition motif is highlighted in black; the IBM-like sequence is highlighted in pink; and the region used for AlphaFold3 prediction is shown in red.

(C) IBM-like sequence in Drice. The propeptide cleavage site of Drice is indicated by a black dashed line; the caspase recognition motif is highlighted in black; the IBM-like sequence is highlighted in pink; and the region used for AlphaFold3 prediction is shown in red.

(D) Predicted complex structure of Bruce BIR and Dcp-1 IBM-like sequence. The AlphaFold3 prediction [model 0] is shown. The Bruce β-X2 and BIR domains are displayed as surfaces in green and pink, respectively. Dcp-1 is shown in stick representation and color-coded according to pLDDT scores, as indicated in the figure. See also panel (F).

(E) Predicted complex structure of Bruce BIR and Drice IBM-like sequence. The AlphaFold3 prediction [model 0] is shown. The Bruce β-X2 and BIR domains are displayed as surfaces in green and pink, respectively. Drice is shown in stick representation and color-coded according to pLDDT scores, as indicated in the figure. See also panel (G).

(F) pLDDT scores of Dcp-1 in the five predicted complex structures with Bruce. For all five AlphaFold3 models, per-residue pLDDT scores of Dcp-1 are plotted. Prediction confidence is color-coded as follows: very high (pLDDT > 90) in dark blue, confident (90 > pLDDT > 70) in light blue, low (70 > pLDDT > 50) in yellow, and very low (pLDDT < 50) in orange.

(G) pLDDT scores of Drice in the five predicted complex structures with dBruce. For all five AlphaFold3 models, per-residue pLDDT scores of Drice are plotted. Prediction confidence is color-coded as follows: very high (pLDDT > 90) in dark blue, confident (90 > pLDDT > 70) in light blue, low (70 > pLDDT > 50) in yellow, and very low (pLDDT < 50) in orange.

(H) Co-immunoprecipitation of N-terminally 3xFLAG-tagged N-terminal region of Bruce (Br, 1–900 aa; containing LD, BIR, and WD40 domains) with C-terminally myc-tagged, catalytically inactive Dcp-1 or Drice (catalytic cysteine mutated to glycine; CG) expressed in *Drosophila* S2 cells. N-terminally 3xFLAG-tagged mRuby3 (mRb3) was used as a control. Apoptosis was induced by cycloheximide (CHX) treatment. 3xFLAG-tagged proteins were immunoprecipitated using an anti-3xFLAG antibody.

903 **Figure EV4**

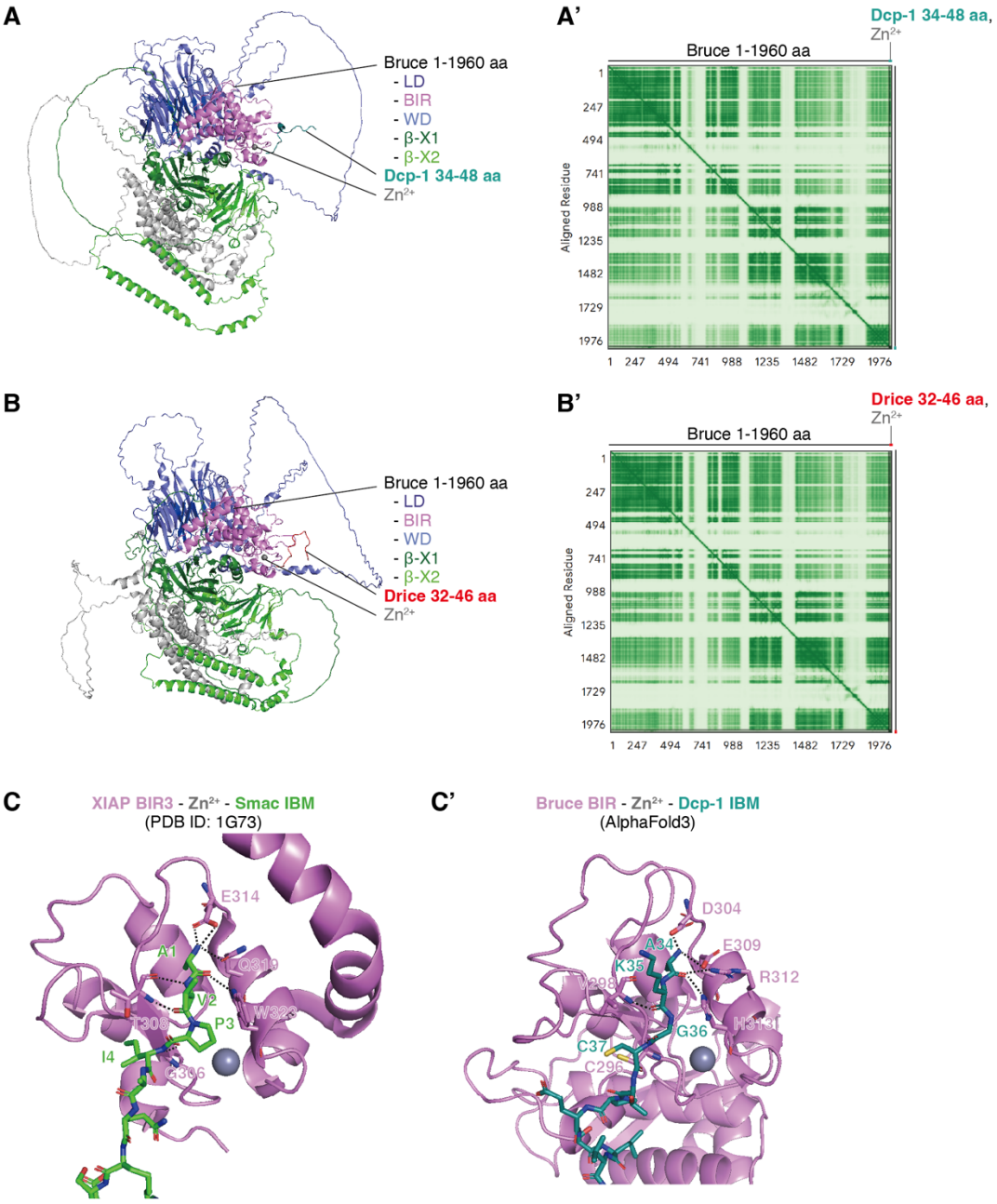

904

905 **Figure EV4. Predicted structures of Bruce complexed with Dcp-1 and Drice IBM-like**
906 **sequences.**
907 (A) Overall view of the predicted complex structure of Bruce and Dcp-1. Model 0 is shown
908 with the same color scheme as in Figure 4A and B. The predicted position error is shown in
909 (A').
910 (B) Overall view of the predicted complex structure of Bruce and Drice. Model 0 is shown with
911 the same color scheme as in Fig. 4A and C. The predicted position error is shown in (B').
912 (C) Structural comparison between the experimentally determined complex of XIAP BIR3 and
913 Smac IBM (C), and the predicted complex of dBruce BIR and Dcp-1 IBM (C'). XIAP BIR3 is
914 shown as a pink cartoon and the Smac IBM as green sticks (PDB ID: 1G73, right panel). dBruce
915 BIR domain is shown as a pink cartoon and the Dcp-1 IBM as dark green sticks (model 0, left

panel). Zn^{2+} ions are shown as gray spheres. Salt bridges are indicated by black dashed lines, along with the corresponding interacting residues.

Figure 5

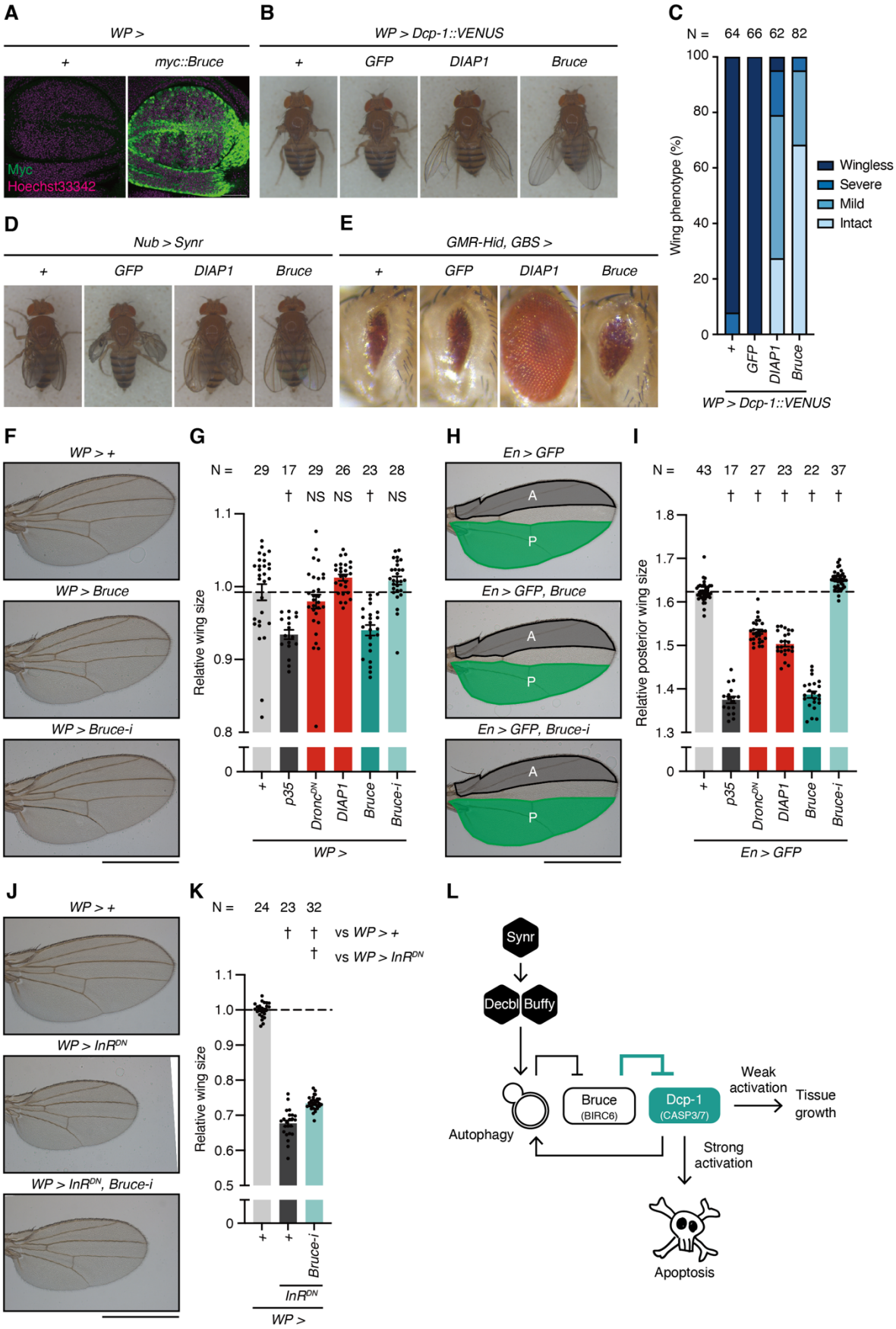
A
WP >
+
myc::Bruce
Myc
Hoechst33342
B
WP > Dcp-1::VENUS
+
GFP
DIAP1
Bruce
C
N = 64 66 62 82
Wing phenotype (%)
Wingless
Severe
Mild
Intact
WP > Dcp-1::VENUS
D
Nub > Synr
E
GMR-Hid, GBS >
F
WP > +
WP > Bruce
WP > Bruce-i
G
N = 29 17 29 26 23 28
† NS NS † NS
Relative wing size
p35
Dronc^DN
DIAP1
Bruce
Bruce-i
WP >
H
En > GFP
En > GFP, Bruce
En > GFP, Bruce-i
A
P
I
N = 43 17 27 23 22 37
Relative posterior wing size
En > GFP
J
WP > InR^DN
WP > InR^DN, Bruce-i
K
N = 24 23 32
vs WP > +
vs WP > InR^DN
InR^DN
L
Synr
Decbl
Buffy
Bruce
(BIRC6)
Dcp-1
(CASP3/7)
Autophagy
Weak activation
Tissue growth
Strong activation
Apoptosis

921 **Figure 5. Bruce selectively suppresses Dcp-1 activity and wing tissue growth.**
922 (A) Expression pattern of overexpressed *myc::Bruce* (green) by using *WP-Gal4* in the wing
923 imaginal discs. Nuclei are visualized using Hoechst 33342 (magenta). Scale bar: 50 μm.
924 (B) Representative images of female wing phenotypes from *Dcp-1::VENUS* overexpression
925 driven by *WP-Gal4* with *DIAP1* or *Bruce* overexpression.
926 (C) Quantification of (B). Each wing is manually classified into four (wingless, severe, mild,
927 and intact) categories. Sample sizes are shown in the figure.
928 (D) Representative images of female wing phenotypes upon *Synr* overexpression driven by
929 *Nub-Gal4* with *DIAP1* or *Bruce* overexpression.
930 (E) Representative images of female eye phenotypes upon *Hid* overexpression with *DIAP1* or
931 *Bruce* overexpression.
932 (F) Representative images of female wing upon *Bruce* or *Bruce-RNAi* (*Bruce-i*) overexpression
933 using *WP-Gal4*. Scale bar: 1 mm.
934 (G) Quantification of relative wing size normalized to the corresponding *No-Gal4* control. Data
935 are presented as mean ± SEM. *p*-values were calculated using one-way analysis of variance
936 (ANOVA) followed by Dunnett's multiple-comparison test against no UAS control. NS, $p \geqq$
937 0.05; †, $p < 0.05$. Sample sizes are shown in the figure.
938 (H) Representative images of female wing upon *Bruce* or *Bruce-RNAi* (*Bruce-i*) overexpression
939 using *En-Gal4*. The grey area (labelled as A) represents the anterior part, and the green area
940 (labelled as P) represents the posterior part of the wing. Scale bar: 1 mm.
941 (I) Quantification of relative posterior part of wing size normalized to corresponding anterior
942 part of wing size. Data are presented as mean ± SEM. *p*-values were calculated using one-way
943 ANOVA followed by Dunnett's multiple comparison test against no UAS control. †, $p < 0.05$.
944 Sample sizes are shown in the figure.
945 (J) Representative images of female wing upon InR^{DN} and *Bruce-RNAi* (*Bruce-i*)
946 overexpression using *WP-Gal4*. Scale bar: 1 mm.
947 (K) Quantification of relative wing size normalized to control (*WP* > +). Data are presented as
948 mean ± SEM. p-values were calculated using one-way ANOVA followed by Sidak's multiple
949 comparison test for selected pairs.†, $p < 0.05$. Sample sizes are shown in the figure.
950 (L) Schematic diagram of Dcp-1 activity-regulating alternative apoptosis signaling pathway in
951 *Drosophila* mediated by autophagy-Bruce axis.
952

953 **Figure EV5**

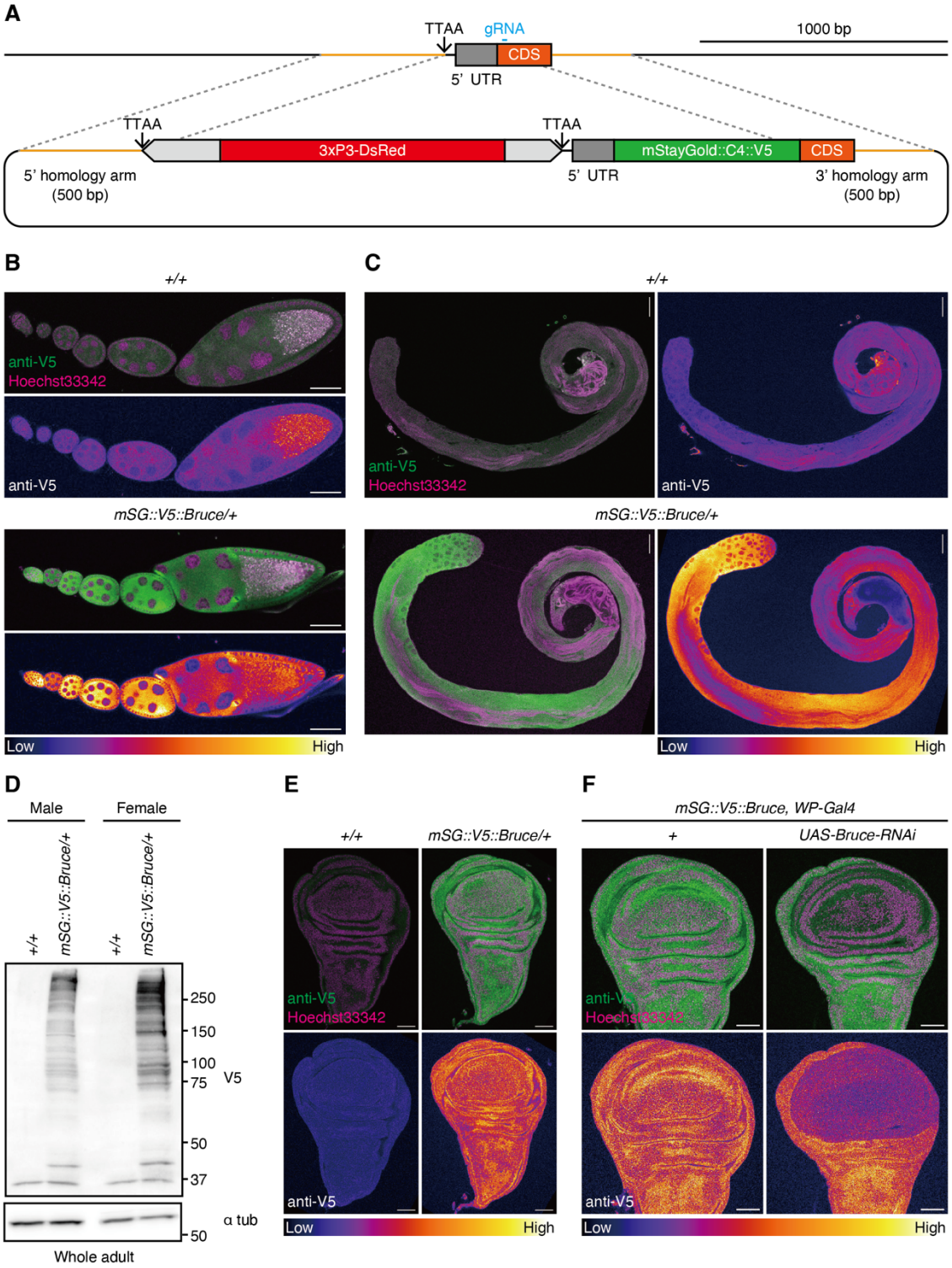

954

955 **Figure EV5. Expression patterns of mStayGold::V5-tag knocked-in Bruce.**

956 (A) Schematic diagram of CRISPR/Cas9-mediated knock-in of mStayGold::C4 linker (C4)::V5
957 tag at the N-terminus of Bruce. A 3xP3-DsRed cassette was integrated at the endogenous TTAA
958 site as a transformation marker. Removal of the cassette restores the genomic TTAA site,
959 enabling scarless genome engineering.

960 (B) Expression pattern of mStayGold (mSG)::C4::V5-tag knocked-in Bruce (green) in the
961 ovariole. Nuclei are visualized using Hoechst 33342 (magenta). Scale bar: 50 µm.
962 (C) Expression pattern of mSG::C4::V5-tag knocked-in Bruce (green) in the testis. Nuclei are
963 visualized using Hoechst 33342 (magenta). Scale bar: 50 µm.
964 (D) Western blotting of expression of mSG::C4::V5-tag knocked-in tagged Bruce in the whole
965 adult male and female.
966 (E) Expression pattern of mSG::C4::V5-tag knocked-in tagged Bruce (green) in the wing
967 imaginal discs. Nuclei are visualized using Hoechst 33342 (magenta). Scale bar: 50 µm.
968 (F) Expression pattern of mSG::C4::V5-tag knocked-in tagged Bruce (green) in the wing
969 imaginal discs upon *Bruce-RNAi* using *WP-Gal4*. Nuclei are visualized using Hoechst 33342
970 (magenta). Scale bar: 50 µm.
971

Legends for Tables

Table EV1. Dcp-1 and Drice proximal protein lists.
Lists of the identified Dcp-1 proximal proteins (abundance ratio (Dcp-1::V5::TurboID/Drice::V5::TurboID) > 2), Drice proximal proteins (abundance ratio (Drice::V5::TurboID/Dcp-1::V5::TurboID) > 2), and candidates for RNAi screening (abundance ratio (Dcp-1::V5::TurboID/Drice::V5::TurboID) > 1.5, abundance ratio (Dcp-1::V5::TurboID/Control) > 10, PSM ≧ 2). The UniProt accessions, gene description, abundance ratio, and # PSMs are listed.

Table EV2. Fly stock list.
List of fly strains. Genotypes, maps, source or references, and stock numbers are listed.

Table EV3. Detailed genotypes.
Detailed genotypes and their related figure # are presented.

Table EV4. Liquid chromatography (LC) settings.
Gradient settings for LC analysis are presented.

Table EV5. Tandem mass spectrometry (MS/MS) settings.
Settings used for the MS/MS analysis are presented.

Table EV6. Proteome Discoverer 2.2 settings.
Proteome Discoverer 2.2 settings for proteomics analysis are presented.